# Mechanisms for the Asymmetric Motion of Submerged Aquatic Vegetation in Waves: A ConsistentMass Cable Model

# Mechanisms for the asymmetric motion of submerged aquatic vegetation in waves: A consistent-mass cable model

**Longhuan Zhu[1], Qing-Ping Zou[2], Kimberly Huguenard[1], and David W. Fredriksson[3]**

[1]Department of Civil and Environmental Engineering, University of Maine, Orono, ME, USA
[2]The Lyell Centre for Earth and Marine Science and Technology, Institute for Infrastructure and Environment, Heriot-Watt University, Edinburgh, UK
[3]Department of Naval Architecture and Ocean Engineering, U.S. Naval Academy, Annapolis, MD, USA

**Key Points:**

- Simulations for the motion of flexible blades in waves with and without currents are improved by using a consistent-mass cable model
- Blade motion is asymmetric due to blade deflection and vertical wave velocity but symmetric if blade length is far less than the wavelength
- Peak asymmetry of vegetation blade motion increases with wave height and blade length but decreases with increasing blade flexural rigidity

Corresponding author: Longhuan Zhu, longhuan.zhu@maine.edu

## Abstract

Submerged aquatic vegetation (SAV) provides primary products for the food web, as well as shelter and nursery for many juvenile species. SAV can also attenuate waves, stabilize the seabed and improve water quality. These environmental services are influenced by the dynamic motion of SAV. In this paper, a consistent-mass cable model was developed to investigate flow interaction with a flexible vegetation blade. Compared with previous vegetation models, the cable model showed improvements in simulating blade motions in waves with and without currents, especially for "second-normal-mode-like" blade motion. Wave asymmetry would cause blade motion to be asymmetric. However, asymmetric blade motion may also occur in symmetric waves. Results indicate that the asymmetric blade motion in symmetric waves is induced by two major mechanisms: (i) the spatial asymmetry of the encountered wave orbital velocities (wave motion relative to blade) due to blade displacements and (ii) the asymmetric action on the blade by vertical wave orbital velocities. Consequently, the blade motion is asymmetric even underneath symmetric waves unless (i) blade length ($l$) is much smaller than the wavelength ($l/L \ll 1$), (ii) blade length is much smaller than the water depth ($l/h \ll 1$) in finite-water-depth waves, or (iii) water depth is much smaller than the wavelength ($h/L \ll 1$). Peak asymmetric blade motion occurs as $l/L$ increases to a critical value. The peak asymmetry increases with wave height and blade length but decreases with increasing blade flexural rigidity. Blade motion characteristics play an important role in wave-vegetation interaction, wave-driven currents, wave-attenuation capacity, breakage of vegetation and ecosystem services.



## Plain Language Summary

Submerged aquatic vegetation (SAV) can reduce wave energy, stabilize the seabed and improve water quality. These environmental services are influenced by SAV motion. In this paper, a numerical model was developed to study flow interaction with a flexible blade. Compared with previous vegetation models, the cable model showed improvements in simulating blade motions in waves with and without currents. Wave asymmetry would cause blade motion to be asymmetric. However, asymmetric blade motion may also occur in symmetric waves. Results indicate that the asymmetric motion in symmetric waves is induced by two major factors: (i) the spatial asymmetry of the encountered wave velocities (wave motion relative to blade) due to blade displacements and (ii) the asymmetric action on the blade by vertical wave velocities. Consequently, the blade motion is asymmetric unless (i) blade length is much smaller than the wavelength, (ii) blade length is much smaller than the water depth in non-deep-water waves, or (iii) water depth is much smaller than the wavelength. Peak asymmetric blade motion increases with wave height and blade length but decreases with increasing blade flexural rigidity. Blade motion characteristics play an important role in wave-vegetation interaction, wave-driven currents, wave-attenuation capacity, breakage of vegetation and ecosystem services.


## 1 Introduction

Submerged aquatic vegetation (SAV) including salt-marshes, seagrass beds, and kelp forests, provides a wide range of ecosystem services. SAV can attenuate wave energy, mitigate coastal erosion, reduce storm damage, and create habitats for fish and shellfish (Dalrymple et al., 1984; Kobayashi et al., 1993; Mendez & Losada, 2004; Lowe et al., 2007; Nepf, 2012; Z. Hu et al., 2014; Ondiviela et al., 2014; Arkema et al., 2015; Guannel et al., 2015; Maza et al., 2015; K. Hu et al., 2018; J. Hu et al., 2019; Suzuki et al., 2019). The storm attenuation capacity of SAV needs to be quantified to develop effective and resilient coastal protection, management and adaptation strategies. While the effectiveness of SAV in coastal protection is dependent

on its coastal coverage, population, size and density, the dynamics of a single blade in waves is critical to the understanding of the hydrodynamics and morphodynamics within a vegetation meadow. The dynamic motion of vegetation changes the flow and produces eddies which, in turn, alter the flow forcing on the blade and blade motion. The blade motion due to flexibility reduces the relative velocity between flow and vegetation as well as the frontal area, resulting in a reduced drag that decreases velocity attenuation and wave attenuation in the vegetation meadow (Bouma et al., 2005; Mullarney & Henderson, 2010; Riffe et al., 2011; Paul et al., 2012; Zeller et al., 2014; Houser et al., 2015; Rupprecht et al., 2017; Abdolahpour et al., 2018). Numerical models have been developed to solve a force balance equation for the vegetation motion, considering gravity, buoyancy, structural damping, bending stiffness as restoring forces, as well as drag and inertia as driving forces (Ikeda et al., 2001; Zeller et al., 2014; Zhu & Chen, 2015; Luhar & Nepf, 2016; Leclercq & de Langre, 2018).

Blade motion in waves can be symmetric or asymmetric. Symmetric motion is a horizontal oscillation over the wave period with near equal bending angles about the vertical axis. Asymmetric motion is an oscillation with more bending in the direction of wave propagation. This asymmetric behavior was described as a "whip-like" response by Rupprecht et al. (2017). Asymmetric blade motion could also induce drag asymmetry with less drag under the wave crest than the trough. According to Luhar et al. (2010, 2013), this effect could enhance the mean flow in the direction of wave propagation. Enhanced mean flow could also reinforce the asymmetry of the blade motion in a meadow (Luhar et al., 2017). Blade inclination in the direction of wave propagation in a meadow may also provide "shelter" effects for sediment and further reduce bedload transport and stabilize the seabed (Rupprecht et al., 2017).

Asymmetric motion of a single blade has been identified in laboratory experiments (e.g., Lei & Nepf, 2019b; Jacobsen et al., 2019). Döbken (2015) attribute the asymmetric behavior of blade motion to that of orbital velocities assuming the blade motion exactly follows the wave excursion. This interpretation only holds when the blade deflection is comparable to wave excursion. Using a numerical model of a single blade, Gijón Mancheño (2016) concluded that the vertical component of wave orbital velocity is the major contributing factor for the asymmetric blade motion based on the results that the blade motion is symmetric once the vertical component of wave orbital velocity is removed. Wave orbital asymmetry caused by wave nonlinearity, bottom slope, bottom friction and the presence of a structure (Elgar et al., 1990; Zou et al., 2003; Peng et al., 2009; Zou & Peng, 2011) also leads to asymmetric response. For instance, this asymmetric motion was observed in a set of laboratory experiments by Luhar and Nepf (2016) conducted with horizontal wave velocities having greater values under the wave crest rather than the trough. Also, with experimental techniques, Rupprecht et al. (2017) observed a transition from symmetric to asymmetric blade motion with increasing wave orbital velocities, which indicates that the asymmetric motions of *Puccinellia* and *Elymus* only occur when the wave orbital velocities reached critical values. Since previous work focused on the influence of wave forcing characteristics that produces asymmetric motion, a need now exists to investigate the role of blade characteristics, including geometry and flexural rigidity that produces similar behavior.

The objective of this work is to identify the mechanisms for the asymmetric motion of SAV with focus on blade geometric and material properties. A cable model with consistent-mass properties is developed to examine the blade motion as a function of blade geometry and wave properties. The cable model is compared with experimental data and previous vegetation models for the large-amplitude motions of blades in waves with and without currents. With the cable model, the theory for the symmetric and asymmetric motion of a flexible blade is developed. The model is then used to investigate the effects of blade length and flexural rigidity as well as wave

height and wave period on the symmetric and asymmetric blade motions. Finally, the mechanisms for asymmetric blade motion and the conditions in which the asymmetry becomes negligible as well as the properties and implications of asymmetric blade motion are discussed.

## 2 Methodology

The wave-induced motion of a flexible blade is often characterized by large deflections which are difficult to resolve with analytical approaches. Therefore, recent studies of blade dynamics have focused on numerical techniques such as the finite-difference and finite-element methods to consider large-deflection-induced geometric nonlinearity. Using a spring-mass model to consider blade rigidity, Zeller et al. (2014) reduced the governing equations of blade dynamics to a system of ordinary differential equations (ODEs). In order to improve the model accuracy, consistent-mass models with partial differential equations (PDEs) were introduced to model the vegetation motion. The vegetation models developed by Luhar and Nepf (2016) and the elastic-rod model coupled with RANS-VOF Navier-Stokes solver proposed by Chen and Zou (2019) perform better for simulating the "first-normal-mode-like" blade motion rather than the "second-normal-mode-like" blade motion. To capture the "second-normal-mode-like" blade motion properly in this study, the consistent-mass cable model developed to represent the dynamics of flexible slender structures including steel cables (Howell, 1992; Triantafyllou & Howell, 1994; Tjavaras et al., 1998), risers (Chatjigeorgiou, 2008), and mooring lines (Li et al., 2018) is extended to simulate the motions of SAV.

### 2.1 2D Cable model

To apply the 2D cable model, an individual blade of SAV was treated as a slender structure fixed at the base and free at the tip as shown on Fig. 1(a). A fixed

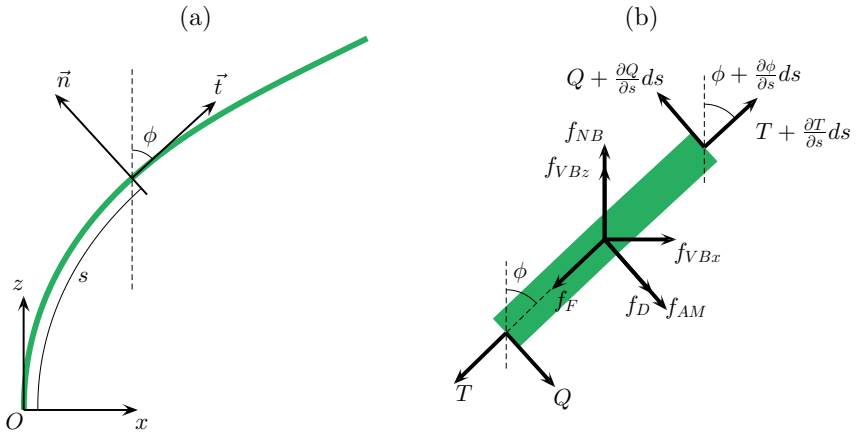


**Figure 1.** Schematic diagram for the coordinate systems and the free-body diagram. (a) Fixed global Cartesian reference frame $(x, z)$ with origin at the blade base. A local Lagrangian coordinate system $(\vec{t}, \vec{n})$ along the blade length $(s)$ associated with the angle of $\phi$ between the tangential direction $(\vec{t})$ and the vertical direction $(z)$. (b) The free-body diagram for one segment of flexible blade $ds$ with effective tension $(T)$, shear $(Q)$, net buoyancy $(f_{NB})$, drag $(f_D)$, friction $(f_F)$, virtual buoyancy $(f_{VBx}, f_{VBz})$, and added mass force $(f_{AM})$.

global Cartesian reference frame $(x, z)$ with the origin at the blade base is defined on Fig. 1(a), where $x$ and $z$ indicate the horizontal and vertical directions, respectively.

The flow field is described by the horizontal and vertical components, $U(x,z,t)$ and $W(x,z,t)$, where $t$ denotes time. To derive the governing equations for the blade motion, a local Lagrangian coordinate system $(\vec{t},\vec{n})$ along the blade length is used with $\vec{t}$ representing the blade-tangential direction and $\vec{n}$ as the blade-normal direction. The velocity components of the blade segment $(ds)$ in the blade-tangential direction and the blade-normal direction are $u$ and $w$, respectively. The distance along the length of the blade $(l)$ from the base is defined as $s$ such that $s = l$ at the tip of the blade. The local bending angle of the blade relative to the vertical direction $(z)$ is $\phi$, where $\phi = 0$ denotes a vertical upright posture for defining symmetric or asymmetric motion. The points in the Lagrangian coordinate system $(\vec{t},\vec{n})$ can be obtained by rotating the global Cartesian coordinates $(x,z)$ counterclockwise by $(\pi/2-\phi)$.

Blade dynamics are governed by the force and momentum balances given by

$$\rho_v bd\left(\frac{\partial u}{\partial t}+w\frac{\partial \phi}{\partial t}\right)=Q\frac{\partial \phi}{\partial s}+\frac{\partial T}{\partial s}+f_{NB}\cos\phi+f_{VBx}\sin\phi+f_{VBz}\cos\phi-f_F, \quad (1)$$

$$\rho_v bd\left(\frac{\partial w}{\partial t}-u\frac{\partial \phi}{\partial t}\right)=\frac{\partial Q}{\partial s}-T\frac{\partial \phi}{\partial s}+f_{NB}\sin\phi-f_{VBx}\cos\phi+f_{VBz}\sin\phi-f_D-f_{AM}, \quad (2)$$

and

$$Q=EI\frac{\partial^2\phi}{\partial s^2}, \quad (3)$$

as well as the compatibility relations for geometrical continuity given by

$$\frac{\partial u}{\partial s}+w\frac{\partial \phi}{\partial s}-\frac{1}{Ebd}\frac{\partial T}{\partial t}=0, \quad (4)$$

and

$$\frac{\partial w}{\partial s}-u\frac{\partial \phi}{\partial s}+\frac{\partial \phi}{\partial t}=0. \quad (5)$$

In equations (1) to (5), $\rho_v$ is the vegetation density, $b$ is the blade width, $d$ is the blade thickness, $E$ is the elastic modulus, $I = bd^3/12$ is the second moment of the cross-section area of the blade, $T$ is the effective tension in the blade-tangential direction, $Q$ is the shear force in the blade-normal direction, $f_{NB}$ is the net buoyancy force per unit blade length (the following forces are per unit length) acting upward, $f_{VBx}$ and $f_{VBz}$ are the horizontal and vertical components of virtual buoyancy (Denny et al., 1997; Gaylord et al., 2003; Rosman et al., 2013), $f_F$ is the skin friction in the blade-tangential direction, $f_D$ is the drag force, and $f_{AM}$ is the added mass force in the blade-normal direction. The effective tension is the sum of the real tension and the product of the hydrostatic pressure and the cross-section area. The usage of effective tension makes *Archimedes principle* applicable to calculate the buoyancy of the segment that is not completely enclosed in fluid due to the neighboring segment (Sparks, 2009; Howell, 1992; Tjavaras et al., 1998). It should be noted that the hydrostatic pressure should be removed from the effective tension when calculating the real tension.

The static net buoyancy force $f_{NB}$ is defined as the difference of the buoyancy and weight, given by

$$f_{NB}=(\rho-\rho_v)gbd, \quad (6)$$

where $\rho$ is the fluid density, and $g$ is the gravitational acceleration. The hydrodynamic forces on the right-hand side of equations (1) and (2) including virtual buoyancy $(f_{VBx}, f_{VBz})$, drag force $(f_D)$, skin friction $(f_F)$, and added mass force $(f_{AM})$, which are given by modified Morison equations (Morison et al., 1950),

$$f_{VBx}=\rho bd\frac{\partial U}{\partial t}, \quad (7)$$

$$f_{VBz}=\rho bd\frac{\partial W}{\partial t}, \quad (8)$$

$$f_D = \frac{1}{2} C_d \rho b \left| w + U\cos\phi - W\sin\phi \right| \left( w + U\cos\phi - W\sin\phi \right), \tag{9}$$

$$f_F = \frac{1}{2} C_f \rho 2 \left( b + d \right) \left| u - U\sin\phi - W\cos\phi \right| \left( u - U\sin\phi - W\cos\phi \right), \tag{10}$$

and

$$f_{AM} = m_a \frac{\partial}{\partial t} \left( w + U\cos\phi - W\sin\phi \right), \tag{11}$$

where $C_d$ is the drag coefficient, $C_f$ is the skin friction coefficient, $m_a$ is the added mass. The added mass is given by $m_a = C_m \pi b^2/4$ using the cylinder-equivalent blade cross-section following Luhar and Nepf (2016) and $C_m$ is the added mass coefficient.

The boundary conditions for the bottom-rooted blade are set as $u = 0$, $w = 0$ and $\phi = 0$ at the blade base ($s = 0$), as well as $T = 0$, $\partial\phi/\partial s = 0$ and $\partial^2\phi/\partial s^2 = 0$ at the blade tip ($s = l$). The governing equations (1) to (5) are a system of non-linear partial differential equations solved by discretization using a finite difference scheme, the Keller Box method (Keller, 1971; Anderson et al., 2016), which is implicit, second order accurate, single step, unconditionally stable and convergent. The Newton-Raphson iteration method was used to solve the discretized equations.

### 2.2 Hydrodynamic force coefficients

The drag coefficient and added mass coefficient for blades are considered a function of Keulegan-Carpenter number (KC). The KC number is defined as $\mathrm{KC} = U_m T_w / b$, where $U_m$ is the maximum oscillatory flow velocity and $T_w$ is the wave period. Based on datasets for rigid plates in oscillatory flows with $\mathrm{KC} = 1.7 \sim 118.2$ (Keulegan & Carpenter, 1958; Sarpkaya & O'Keefe, 1996), Luhar and Nepf (2016) developed formulas for drag coefficient and added mass coefficient, given by

$$C_d = \max(10\mathrm{KC}^{-1/3}, 1.95) \tag{12}$$

and

$$C_m = \min(C_{m1}, C_{m2}), \tag{13}$$

respectively, where $C_{m1} = \begin{cases} 1 + 0.35\mathrm{KC}^{2/3} & \mathrm{KC} < 20 \\ 1 + 0.15\mathrm{KC}^{2/3} & \mathrm{KC} \geq 20 \end{cases}$ and $C_{m2} = 1 + (\mathrm{KC} - 18)^2/49$ as described in Luhar (2012).

The friction coefficient is taken as a function of Reynolds number (Re). The Reynolds number is defined as $\mathrm{Re} = U_m b/\nu$, where $\nu$ is the kinematic viscosity of the water. According to Zeller et al. (2014) and Abdelrhman (2007), the friction coefficient is given by

$$C_f = 0.074\mathrm{Re}^{-1/5}. \tag{14}$$

Luhar and Nepf (2016) noted that the exact value of $C_f$ had little effect on their model results because the ratio of the calculated root-mean-square forces for $C_f = 0.1$ and $C_f = 0.01$ was distributed with mean and standard deviation $1.00 \pm 0.01$. For simplicity, Zeller et al. (2014) selected an approximated value of 0.02. In contrast, Luhar and Nepf (2016) used a larger value of $C_f = 0.1$ because their model was found unstable for the cases with high Cauchy number if $C_f = 0.01$. The Cauchy number (Ca) is the ratio of the hydrodynamic force to the restoring force due to plant stiffness and given by $\mathrm{Ca} = \rho b U_m^2 l^3/EI$. In this study, equation (14) is used to calculate the friction coefficient.

## 3 Model-data comparison

### 3.1 Blade motion in combined waves and currents

The cable model results were first compared with the laboratory experiments by Zeller et al. (2014) for the blades in combined waves and currents. During the

experiments, six wave-current conditions were produced, where the wave period $T_w = 2.80 \sim 5.19$ s, the amplitude of the horizontal wave velocity $U_w = 9.45 \sim 25.8$ cm/s, and the currents $U_c = 3.66 \sim 13.7$ cm/s (Table 1). The still water depth was 40

**Table 1.** Blade properties and wave conditions in the experiments by Zeller et al. (2014) and Luhar and Nepf (2016).

| Experiments | Blade properties | Waves | | | Currents |
|---|---|---|---|---|---|
| | | $T_w$ [s] | $a_w$ [cm] | $U_w$ [cm/s] | $U_c$ [cm/s] |
| Blade in waves and currents (Zeller et al., 2014) | LDPE: | 5.19 | - | 25.8 | 12.1 |
| | $\rho_v = 920$ kg/m$^3$ | 4.29 | - | 17.3 | 13.2 |
| | $E = 0.3$ GPa | 2.80 | - | 9.45 | 12.9 |
| | $b = 1$ cm | 5.19 | - | 24.4 | 6.00 |
| | $d = 0.2, 0.25, 0.3$ mm | 4.29 | - | 15.9 | 5.63 |
| | $l = 15, 20$ cm | 2.80 | - | 9.64 | 4.77 |
| Blade in waves (Luhar & Nepf, 2016) | 0.4 mm-thick HDPE: | 2 | 1(0.9) | 5.0 | - |
| | $\rho_v = 950$ kg/m$^3$ | 2 | 2(1.9) | 10.1 | - |
| | $E = 0.93$ GPa | 2 | 3(2.9) | 15.4 | - |
| | 1.9 mm-thick silicon foam: | 2 | 4(3.9) | 20.6 | - |
| | $\rho_v = 670$ kg/m$^3$ | 1.4 | 2(1.7) | 8.9 | - |
| | $E = 0.5$ MPa | 1.4 | 4(3.5) | 16.7 | - |
| | $b = 2$ cm | 1.1 | 2(1.7) | 6.6 | - |
| | $l = 5, 10, 15, 20$ cm | 1.1 | 4(3.6) | 12.8 | - |

cm. The model blades were made of low-density polyethylene (LDPE) with $\rho_v = 920$ kg/m$^3$ and $E = 0.3$ GPa (Ghisalberti & Nepf, 2002). Four 1 cm-wide model blades with different lengths and thicknesses were used. Three of the blades were 15 cm long with thicknesses of 0.20, 0.25, and 0.30 mm. The fourth blade was 20 cm long with a thickness of 0.25 mm. Therefore, Ca $= 101 \sim 2883$, KC $= 40 \sim 197$ and Re $= 1441 \sim 3790$. Details of the experiments can be found in Zeller et al. (2014).

To drive the model, the wave-current flow is considered as a superposition of currents and linear waves. The hydrodynamic force coefficients for waves as described in section 2.2 are assumed to be also applicable for combined waves and currents conditions following Lei and Nepf (2019a). The calculated deflected blade-tip heights ($z_T$) at the maximum horizontal displacements ($x_{T,max}$) are shown on Fig. 2 along with the data and the model results from Zeller et al. (2014). The root-mean-square-error (RMSE) for the cable model results is RMSE $= 0.043$ and smaller than that of the model results from Zeller et al. (2014) with RMSE $= 0.103$. The improvement of RMSE is possible because the present cable model is a consistent-mass model while the Zeller et al. (2014) model is a spring-mass model. Additionally, the compatibility relations described in equation (4) and (5) are not included in Zeller et al. (2014). Therefore, the Zeller et al. (2014) model has difficulty to converge for some test cases with large Ca $\gg 10^3$ (e.g., missed points on Fig. 2), where the blade is so flexible that can curl over. In comparison, the cable model is stable and convergent for all the test cases.

### 3.2 Blade motion in waves

The cable model results were also compared with the data from the laboratory experiments by Luhar and Nepf (2016) for waves only. Eight wave conditions were produced with wave period $T_w = 1.1 \sim 2.0$ s and wave amplitude $a_w = 1 \sim 4$ cm (Table 1). The still water depth ($h$) was 30 cm. The model blades were made of

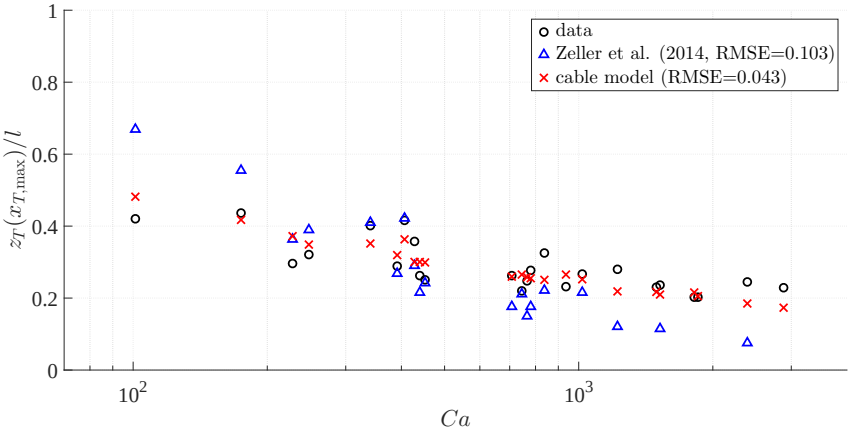


**Figure 2.** Model-data comparison for the normalized deflected blade-tip height ($z_T/l$) at the maximum horizontal displacement of the blade tip ($x_{T,max}$) vs the Cauchy number (Ca). The data is denoted by black circles, the model results from Zeller et al. (2014) are denoted by blue triangles and those from the cable model are denoted by red crosses. The associated root-mean-square-error (RMSE) is shown in the legend.

high-density polyethylene (HDPE, $\rho_v = 950$ kg/m$^3$ and $E = 0.93$ GPa) and silicon foam ($\rho_v = 670$ kg/m$^3$ and $E = 0.5$ MPa). The blades were 2 cm wide with lengths of 5, 10, 15, and 20 cm. The thicknesses were 0.4 mm and 1.9 mm for the HDPE and silicon foam blades, respectively. Therefore, Ca $= 0.02 \sim 1200$, KC $= 3.7 \sim 20.6$, and Re $= 1000 \sim 4120$. Details of the experiments can be found in Luhar and Nepf (2016).

The velocity profile was measured using particle image velocimetry (PIV, details referred to Luhar & Nepf, 2016) that captures the instantaneous flow velocity resulting from the superposition of the incident and reflected waves, where the wave reflection ratio of the wave flume is 7% (Lei & Nepf, 2019b). The first four harmonics fit of the measured flow velocity ($r^2 = 0.99$, Fig. 3) at one horizontal position was used as an approximation for the input flow field in Luhar and Nepf (2016). This approximation only represents the temporal variation of the velocity profile at that horizontal position. Due to the effects of wave reflection on the velocity amplitude, this approximation for the flow profile at other horizontal position may has a small $r^2 = 0.91$ for the wave reflection of 7%. To represent the spatial variation of the wave flow field, the wave number ($k$) is used and obtained by solving the dispersion relation, $\omega^2 = gk \tanh kh$ (Dean & Dalrymple, 1991), where the wave radian frequency $\omega = 2\pi/T_w$. By incorporating the effects of the spatial variance into the wave phase, the modified approximation for the input flow field reduces the effects of wave reflection on the flow field and enhances $r^2$ to be greater than 0.98 at all the horizontal positions in the range of the blade motion. In addition, the wave reflection-induced change of the velocity amplitude at all the horizontal positions has limited effects ($< 2.5\%$) on the drag coefficient. Therefore, the modified approximation for the input flow field by incorporating spatial variance is adequately precise to drive the cable model.

The comparisons between the cable model results and the data, as well as the model results from Luhar and Nepf (2016) are shown on Fig. 4 for the horizontal displacement range of the blade-tip ($x_{T,max} - x_{T,min}$) and the root-mean-square of the total horizontal force ($F_{x,rms}$) at the blade base. To normalize $F_{x,rms}$, the root-mean-square of the total horizontal force on a rigid blade with the same geometry is

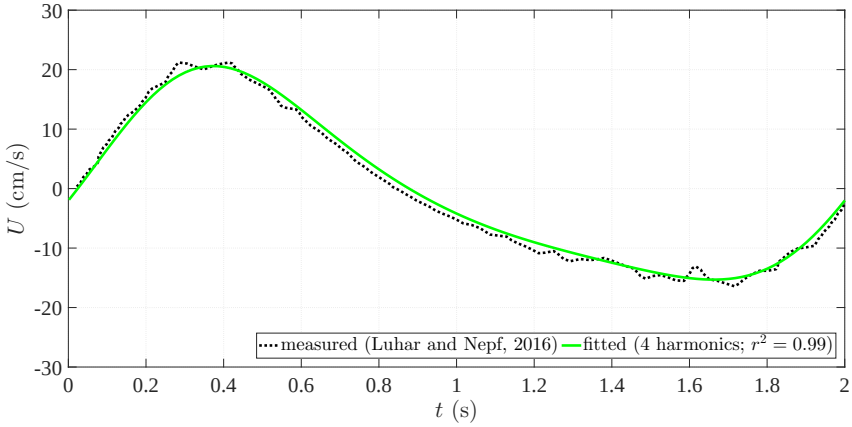


**Figure 3.** Measured horizontal component of the wave orbital velocity at $z = 0$ for the wave with period $T_w = 2$ s and amplitude $a_w = 4$ cm (Luhar & Nepf, 2016). The measured horizontal component of the wave orbital velocity is denoted by the dotted black line and the first four harmonics fit is denoted by solid green line.

used and given by

$$F_{x,rms,rigid} = \sqrt{\frac{1}{T_w}\int_0^{T_w}\left[\int_0^l \left(\frac{1}{2}C_d\rho b|U|U + \rho m_a\frac{\partial U}{\partial t} + \rho bd\frac{\partial U}{\partial t}\right)dz\right]^2 dt}. \qquad (15)$$

For the HDPE blades, the RMSE of the cable model results is 0.050 for the blade-tip range and 0.184 for the total horizontal force, which are a little larger than those of the model results from Luhar and Nepf (2016) with RMSE = 0.048 for the blade-tip range and RMSE = 0.174 for the total horizontal force. However, the cable model shows improvements in simulating the motion of the silicon foam blade with RMSE = 0.126 for the blade-tip range and RMSE = 0.043 for the total horizontal force, which are smaller than those by the model of Luhar and Nepf (2016) with RMSE = 0.151 for the blade-tip range and RMSE = 0.049 for the total horizontal force.

To further evaluate the performance of the numerical models, the model results for the blade tip trajectory are shown on Fig. 5 (see Movie S1 for the comparison at each time step in supporting information) and the blade postures associated with the total horizontal force ($F_x$) are shown on Fig. 6 and Fig. 7. We note that the blade motion shown on Fig. 5 is asymmetric with respect to the vertical line $x = 0$, which will be further examined in section 4.

Both model blades exhibit periodic motion, but with different dynamic characteristics. For instance, the HDPE model blade behaves like the "first normal mode" of a cantilever beam (Fig. 5a and Fig. 6a-l) since the wave frequency $f_w = 1/T_w = 0.5$ Hz is smaller than the first natural frequency $f_1 = 1.875^2 f_0 = 1.54$ Hz of the HDPE blade, where $f_0 = \sqrt{EI/[(\rho_v bd + m_a)l^4]}$ (Rao, 2010). The silicon foam model blade, however, behaves like a "second normal mode" (Fig. 5b and Fig. 7a-l) since the wave frequency $f_w$ is between the first natural frequency $f_1 = 0.36$ Hz and the second natural frequency $f_2 = 4.694 f_0 = 2.26$ Hz of the silicon foam blade. The normal mode theory for linear vibration is not suitable to analyze the nonlinear vibration of the blades, but it is the basis to analyze the nonlinear normal mode for large-amplitude vibration of a cantilever beam (Hsieh et al., 1994).

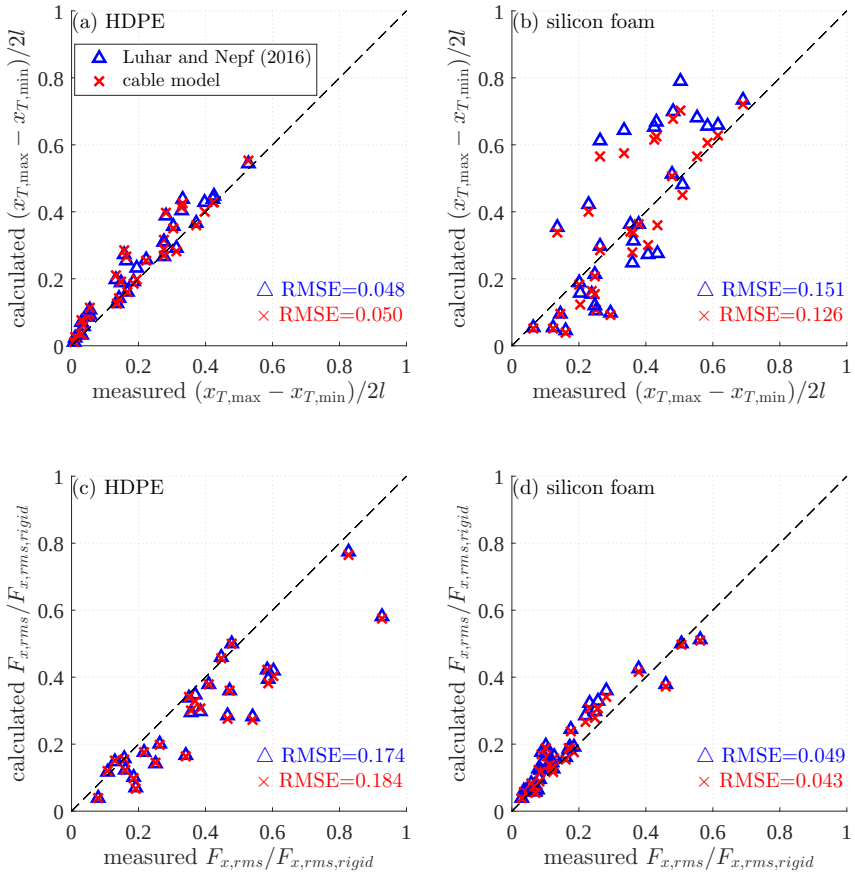


**Figure 4.** Comparisons for (a, b) the normalized horizontal displacement range of the blade-tip $(x_{T,max} - x_{T,min})/2l$ and (c, d) the root-mean-square of the total horizontal force $(F_{x,rms})$ normalized by the total horizontal force $(F_{x,rms,rigid})$ for a rigid blade with the same geometry for (a, c) HPDE and (b, d) silicon foam blades, respectively. The model results from Luhar and Nepf (2016) are denoted by blue triangles with root-mean-square-error (RMSE) in blue text while the cable model results are denoted by red crosses with RMSE in red text.

To quantify the performance of the numerical simulations for blade postures, the normalized error $(\epsilon_T)$ between the simulated and observed displacements of the blade tip is used and given by

$$\epsilon_T(t) = \sqrt{(x_T - x_T^*)^2 + (z_T - z_T^*)^2}/l, \tag{16}$$

where $(x_T, z_T)$ and $(x_T^*, z_T^*)$ are the simulated and observed Cartesian coordinates of the blade tip, respectively. A smaller value of $\epsilon_T$ indicates a closer simulation. For the HDPE blade shown on Fig. 6(m), $\epsilon_T$ of the cable model results is smaller than that of the model results from Luhar and Nepf (2016) under wave trough. The time averaged $\epsilon_T$ over one wave period for the cable model is $\overline{\epsilon_T} = 0.116$ and 14.1% less than that of the model from Luhar and Nepf (2016) with $\overline{\epsilon_T} = 0.135$ for HDPE blade (Table 2). For the silicon foam blade shown on Fig. 7(m), $\epsilon_T$ of the cable model is smaller than that of the model from Luhar and Nepf (2016) during the entire wave period. The $\overline{\epsilon_T}$ of the cable model is 0.056 and 79.7% less than that of the model from Luhar and Nepf (2016) with $\overline{\epsilon_T} = 0.276$ for silicon foam blade (Table 2).

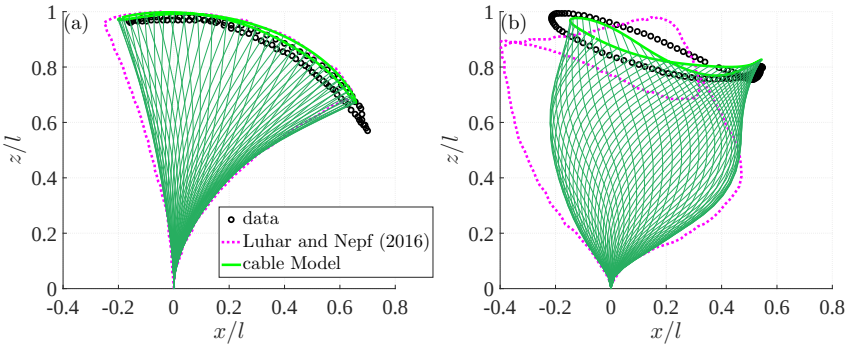


**Figure 5.** Blade postures and blade tip trajectory for the 20 cm-long (a) HDPE and (b) silicon foam blades over one wave period for the waves with period $T_w = 2$ s and amplitude $a_w = 4$ cm. The data is denoted by black open circles, the model results from Luhar and Nepf (2016) are denoted by magenta dotted lines, and those from the cable model are denoted by green lines (thick green lines indicate the trajectory of the blade tip while the thin green lines indicate the postures of the blade at selected time steps).

**Table 2.** Normalized time averaged error ($\overline{\epsilon_T}$) for the simulated displacements of the blade tip.

| Blades | Luhar and Nepf (2016) (a) | Cable model (b) | (a-b)/a × 100% |
|---|---|---|---|
| silicon foam | 0.276 | 0.056 | 79.7% |
| HDPE | 0.135 | 0.116 | 14.1% |

The calculated total horizontal force by the cable model is consistent with the data with a normalized root-mean-square error (NRMSE) of 0.151 for the HDPE blade and 0.045 for the silicon foam blade. The NRMSE of $F_x$ by the cable model is comparable to the model results from Luhar and Nepf (2016) with NRMSE = 0.139 for the HDPE blade and NRMSE = 0.041 for the silicon foam blade. Although the results of the two models are quite different for the blade postures, the results for the total horizontal force are similar because the total horizontal force is the integration of the horizontal force distributed along the blade. The variance of the distributed force and the momentum along the blade cannot be represented by the total horizontal force, but it imposes significant influences on the blade postures. Therefore, the difference in the total horizontal force comparison with the results from Luhar and Nepf (2016) is small, but the difference in posture comparison is large. As the postures of the blade represent the combined action of the distributed force and momentum along the blade, the posture is used to demonstrate the blade dynamics rather than the integration of the horizontal forces along the blade length.

Compared with the model of Luhar and Nepf (2016), the cable model showed an advantage to simulate the blade dynamics, in particular for the simulations of blade postures in waves. The improvements for the posture simulations are mainly due to the incorporation of (i) the influences of the blade-motion-induced rotations of local Lagrangian coordinates along the blade on the added mass force as shown in equation (11), (ii) the dynamic equilibrium for the geometric continuity of the segments as shown in the compatibility relations from equations (4) and (5), and (iii) the spatial variation of the wave orbital velocity encountered by the blade due to blade displacements. Since the blade acts as a solid moving boundary in the fluid domain, its motion influences the flow structure. Therefore, accurate blade posture predictions are required to fully

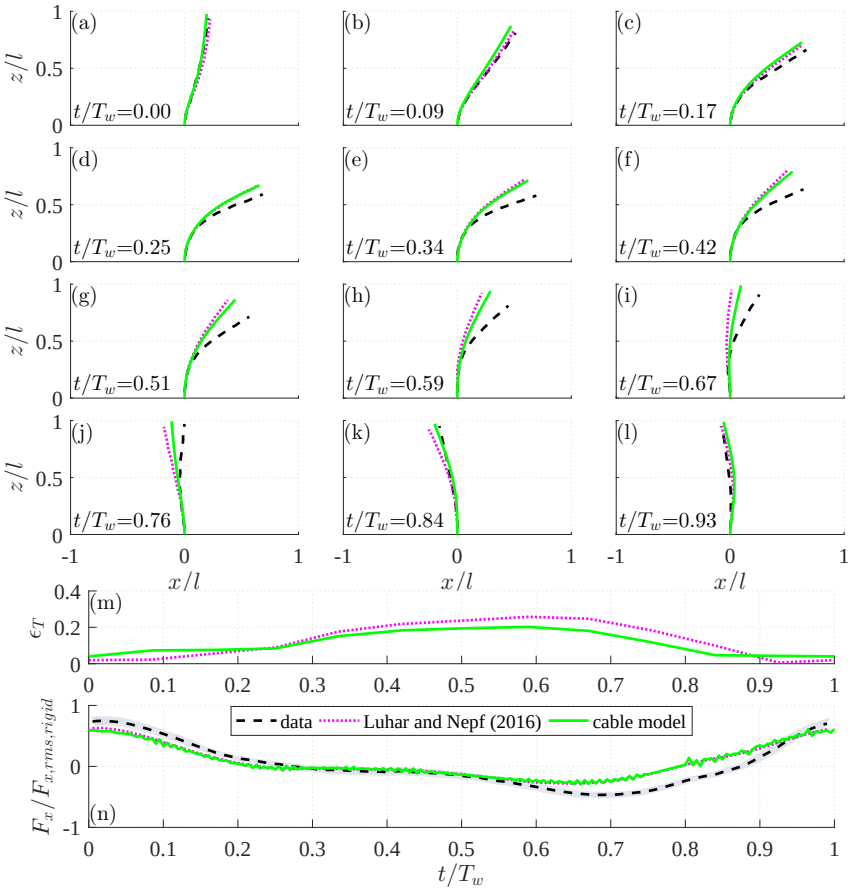


**Figure 6.** Comparisons for (a-l) the 20 cm-long HDPE blade posture $(x, z)$ normalized by blade length $(l)$, (m) the differences between the simulated and observed blade-tip displacements $(\epsilon_T)$, and (n) the total horizontal force $(Fx)$ normalized by the root-mean-square horizontal force by rigid plate with the same geometry $(F_{x,rms,rigid})$ along time $(t)$. The waves with period $T_w$ = 2 s and amplitude $a_w$ = 4 cm propagate from left to right. Black dashed lines: the data from Luhar and Nepf (2016); magenta dotted lines: the model results from Luhar and Nepf (2016); green solid lines: the cable model results; grey shaded region: the estimated uncertainty in the experiments (Luhar & Nepf, 2016).

resolve the flow-vegetation interaction, wave-driven currents in a vegetation meadow, and the wave attenuation by vegetation. This model can also be used to estimate the internal stress of the blade and the total force at the bottom of the blade in order to analyze the breakage and the sediment holding properties of the blade.

## 4 Symmetric and asymmetric blade motions

### 4.1 Definition

To quantify the asymmetric motion, the blade posture asymmetry $(\beta_{xT})$ is defined as the ratio of the time-averaged horizontal displacement of the blade tip $(\overline{x_T})$ to the maximum absolute horizontal displacement $(|x_T|_{\max})$ over one wave period (Fig. 8) and given by

$$\beta_{xT} = \frac{\overline{x_T}}{|x_T|_{\max}}, \tag{17}$$

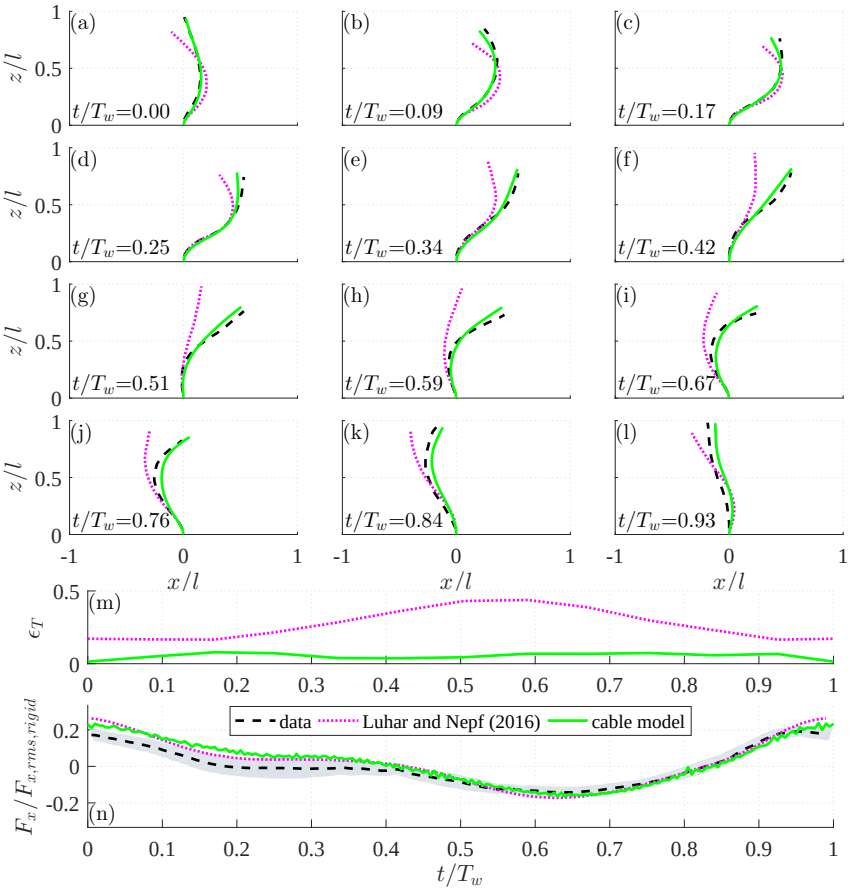


**Figure 7.** Comparisons for (a-l) the 20 cm-long silicon foam blade posture $(x, z)$ normalized by blade length $(l)$, (m) the differences between the simulated and observed blade-tip displacements $(\epsilon_T)$, and (n) the total horizontal force $(Fx)$ normalized by the root-mean-square horizontal force by rigid plate with the same geometry $(F_{x,rms,rigid})$ along time $(t)$. The waves with period $T_w = 2$ s and amplitude $a_w = 4$ cm propagate from left to right. Black dashed lines: the data from Luhar and Nepf (2016); magenta dotted lines: the model results from Luhar and Nepf (2016); green solid lines: the cable model results; grey shaded region: the estimated uncertainty in the experiments (Luhar & Nepf, 2016).

where $(\overline{x_T})$ is always smaller than $(|x_T|_{\max})$ such that $\beta_{xT} \in (-1, 1)$. The posture asymmetry is positive when the blade inclines to the direction of wave propagation. For example, the motions of the blades shown on Fig. 5 are asymmetric with $\beta_{xT} = 0.30$ and $\beta_{xT} = 0.27$ for HDPE and silicon foam blades, respectively.

### 4.2 Theory

Asymmetric blade motions shown on Fig. 5 are partially induced by the weak asymmetry of wave motion as shown on Fig. 3. However, using linear waves to drive the model without the influences of wave asymmetry still results in asymmetric blade motion (Fig. 9) with $\beta_{xT} = 0.31$ and $\beta_{xT} = 0.32$ for HDPE and silicon foam blades, respectively. The magnitude of the blade posture asymmetry in linear waves is similar to that in weak asymmetric waves, suggesting that other mechanisms may have contributed to the observed asymmetric blade motion.

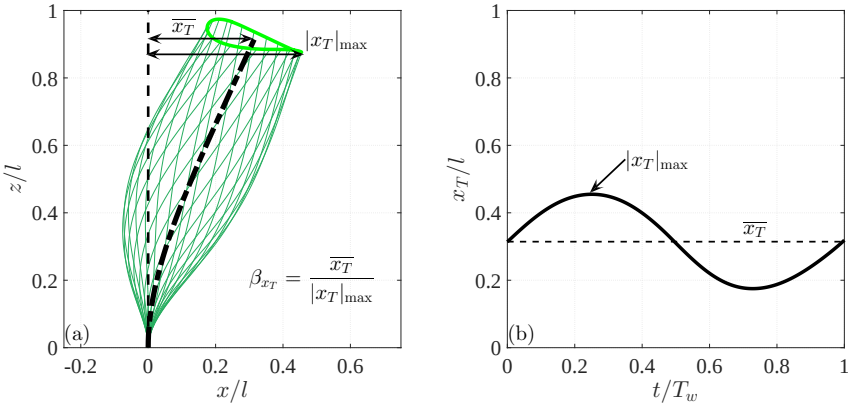


**Figure 8.** The blade posture asymmetry ($\beta_{xT}$) is defined as the ratio of time-averaged displacement of the blade tip ($\overline{x_T}$) to the maximum absolute displacement ($|x_T|_{\max}$). (a) Blade postures and tip trajectory. The horizontal and vertical coordinates $(x, z)$ are normalized by the blade length ($l$). The thin green lines indicate the blade postures and the thick green line indicate the excursion of the blade tip. The black dash-dotted line indicates the time-averaged posture of the blade postures over one wave period and the thin dashed line indicate the vertical center. (b) The time series of the horizontal displacement of the blade tip. The time ($t$) is normalized by wave period ($T_w$).

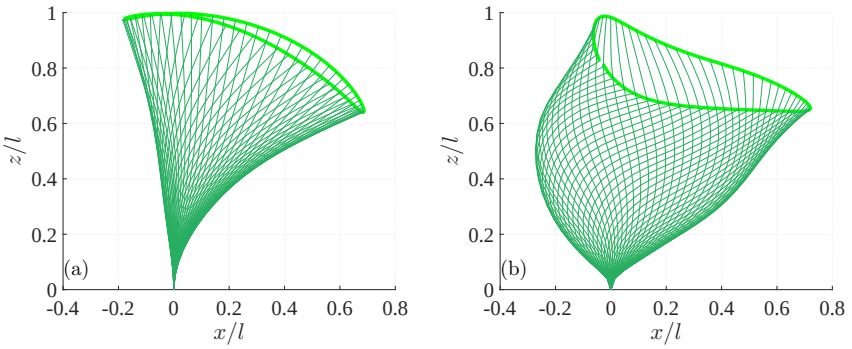


**Figure 9.** Blade postures and blade tip trajectory for the 20 cm-long (a) HDPE and (b) silicon foam blades over one wave period for the symmetric waves with period $T_w$=2 s and amplitude $a_w$=4 cm. Thick green lines indicate the trajectory of the blade tip while the thin green lines indicate the postures of the blade at selected time steps.

The mechanisms that contribute to the blade asymmetric motion in linear waves are identified according to the governing equations of blade motion. Substituting equations (3) and (6) to (11) into (1) and (2) yields

$$\begin{aligned} & EI\frac{\partial\phi}{\partial s}\frac{\partial^2\phi}{\partial s^2} + \frac{\partial T}{\partial s} + (\rho - \rho_v)\, gbd\cos\phi \\ & + \frac{1}{2}C_f\rho 2(b+d)\left|-u + u_w(x,z,t)\right|\left[-u + u_w(x,z,t)\right] \\ & + \rho bd\left[-\frac{\rho_v}{\rho}\left(\frac{\partial u}{\partial t} + w\frac{\partial\phi}{\partial t}\right) + \frac{\partial u_w(x,z,t)}{\partial t} + w_w(x,z,t)\frac{\partial\phi}{\partial t}\right] = 0 \end{aligned} \tag{18}$$

and

$$\begin{aligned}
&EI\frac{\partial^3\phi}{\partial s^3} - T\frac{\partial\phi}{\partial s} + (\rho-\rho_v)\,gbd\sin\phi \\
&+\frac{1}{2}C_d\rho b\,|-w+w_w(x,z,t)|\,[-w+w_w(x,z,t)] \\
&+C_m\frac{\pi}{4}b^2\left[-\frac{\partial w}{\partial t}+\frac{\partial w_w(x,z,t)}{\partial t}\right] \\
&+\rho bd\left[-\frac{\rho_v}{\rho}\left(\frac{\partial w}{\partial t}-u\frac{\partial\phi}{\partial t}\right)+\frac{\partial w_w(x,z,t)}{\partial t}-u_w(x,z,t)\frac{\partial\phi}{\partial t}\right]=0,
\end{aligned} \tag{19}$$

where

$$u_w(x,z,t) = U\sin\phi + W\cos\phi \tag{20}$$

and

$$w_w(x,z,t) = -U\cos\phi + W\sin\phi \tag{21}$$

are the encountered flow velocities (wave motion related to the blade) in the blade tangential and normal direction, respectively. According to linear wave theory (Dean & Dalrymple, 1991), the horizontal and vertical components of the wave orbital velocity are given by

$$U(x,z,t) = a_w\omega\frac{\cosh kz}{\sinh kh}\cos(kx-\omega t) \tag{22}$$

and

$$W(x,z,t) = a_w\omega\frac{\sinh kz}{\sinh kh}\sin(kx-\omega t). \tag{23}$$

Substituting equations (22) and (23) into equations (20) and (21) yields

$$\begin{aligned}
&u_w(x,z,t) \\
=&a_w\omega\frac{\cosh kz}{\sinh kh}\cos\phi\cosh kx\frac{\tan\phi\tan kx-\tanh kz}{\cos\left[kx+\arctan\left(\frac{\tan\phi}{\tanh kz}\right)\right]}\sin\psi_t
\end{aligned} \tag{24}$$

and

$$\begin{aligned}
&w_w(x,z,t) \\
=&a_w\omega\frac{\cosh kz}{\sinh kh}\cos\phi\cosh kx\frac{-1+\tan\phi\tan kx\tanh kz}{\cos\left[kx+\arctan\left(\tan\phi\tanh kz\right)\right]}\cos\psi_n,
\end{aligned} \tag{25}$$

where the velocity phase $\psi_t = \omega t - [kx + \arctan(\tan\phi/\tanh kz)]$ and $\psi_n = \omega t - [kx + \arctan(\tan\phi\tanh kz)]$.

It is assumed that the blade moves at the same period as the wave period ($T_w$). It is also assumed that there is a unique solution to the governing equations (18), (19), (4) and (5). The existence of symmetric motion is explored by examining a pair of symmetric solutions, i.e., $\{T(s,t),\ u(s,t),\ w(s,t),\ \phi(s,t)\}$ at the position $(x,z)$ at time $t$ and $\{T(s,t+\Delta t),\ u(s,t+\Delta t),\ w(s,t+\Delta t),\ \phi(s,t+\Delta t)\}$=$\{T(s,t),\ u(s,t),\ -w(s,t),\ -\phi(s,t)\}$ at the symmetric position $(-x,z)$ at time $t+\Delta t$, as demonstrated on Fig. 10. It takes $\Delta t$ to move from position $(x,z)$ to $(-x,z)$ and it also takes the same time $\Delta t$ to move back to $(x,z)$ due to symmetric motion, yielding $\Delta t = T_w/2$.

Taking $\{T(s,t),\ u(s,t),\ w(s,t),\ \phi(s,t)\}$ as the solution at time $t$, $\{T(s,t),\ u(s,t),\ -w(s,t),\ -\phi(s,t)\}$ is shown to satisfy the compatibility relations by substituting it into the compatibility relation equations (4) and (5). The next step is to check if $\{T(s,t),\ u(s,t),\ -w(s,t),\ -\phi(s,t)\}$ also satisfies equations (18) and (19) at $t+\Delta t$. Substituting $\{T(s,t),\ u(s,t),\ -w(s,t),\ -\phi(s,t)\}$ into equations (18) and (19) for time

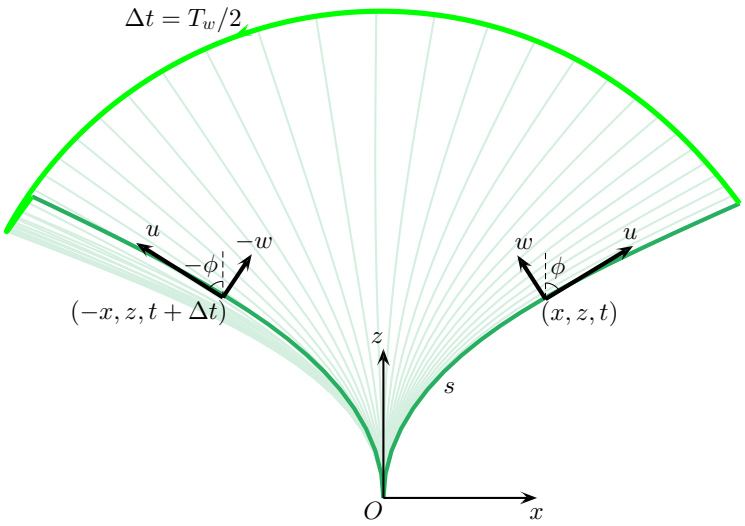


**Figure 10.** The postures of the blade over one-half of a wave period ($\Delta t = T_w/2$) for symmetric motion. The thin arrows show the global coordinate system $(x, z)$ with origin $O$ while the thick arrows show the velocity of the blade segments at the distance of $s$. The thin green lines indicate the selected blade postures. The thick dark green lines indicate the blade posture with velocity $(u, w)$ and bending angle $\phi$ at the position $(x, z)$ at time $t$ and the symmetric blade posture with symmetric velocity $(u, -w)$ and symmetric bending angle $-\phi$ at the symmetric position $(-x, z)$ after half wave period. The thick light green line indicates the excursion of the blade tip.

$t + \Delta t$ yields

$$\begin{aligned} &EI\frac{\partial\phi}{\partial s}\frac{\partial^2\phi}{\partial s^2} + \frac{\partial T}{\partial s} + (\rho - \rho_v)\, gbd\cos\phi \\ &+\frac{1}{2}C_f\rho 2(b+d)\left|-u + u_w(-x, z, t + \frac{T_w}{2})\right|\left[-u + u_w(-x, z, t + \frac{T_w}{2})\right] \\ &+\rho bd\left[-\frac{\rho_v}{\rho}\left(\frac{\partial u}{\partial t} + w\frac{\partial\phi}{\partial t}\right) + \frac{\partial u_w(-x, z, t + \frac{T_w}{2})}{\partial t} - w_w(-x, z, t + \frac{T_w}{2})\frac{\partial\phi}{\partial t}\right] = 0 \end{aligned} \tag{26}$$

and

$$\begin{aligned} &EI\frac{\partial^3\phi}{\partial s^3} - T\frac{\partial\phi}{\partial s} + (\rho - \rho_v)\, gbd\sin\phi \\ &+\frac{1}{2}C_d\rho b\left|-w - w_w(-x, z, t + \frac{T_w}{2})\right|\left[-w - w_w(-x, z, t + \frac{T_w}{2})\right] \\ &+C_m\frac{\pi}{4}b^2\left[-\frac{\partial w}{\partial t} - \frac{\partial w_w(-x, z, t + \frac{T_w}{2})}{\partial t}\right] \\ &+\rho bd\left[-\frac{\rho_v}{\rho}\left(\frac{\partial w}{\partial t} - u\frac{\partial\phi}{\partial t}\right) - \frac{\partial w_w(-x, z, t + \frac{T_w}{2})}{\partial t} - u_w(-x, z, t + \frac{T_w}{2})\frac{\partial\phi}{\partial t}\right] = 0. \end{aligned} \tag{27}$$

The differences between equations (26) and (18), and between equations (27) and (19) are the terms involving flow velocities, $u_w$ and $w_w$. In order for (26) to equal (18) and (27) to equal (19), it requires

$$u_w(-x, z, t + \frac{T_w}{2}) = u_w(x, z, t) \tag{28}$$

and

$$w_w(-x, z, t + \frac{T_w}{2}) = -w_w(x, z, t). \tag{29}$$

Replacing $(x, z, t)$ by $(-x, z, t + \frac{T_w}{2})$ in equations (24) and (25) yields the velocity at $(-x, z, t + \frac{T_w}{2})$, i.e.,

$$\begin{aligned} &u_w(-x, z, t + \frac{T_w}{2}) \\ =&a_w\omega\frac{\cosh kz}{\sinh kh}\cos\phi\cosh kx\frac{\tan\phi\tan kx - \tanh kz}{\cos\left[kx + \arctan\left(\frac{\tan\phi}{\tanh kz}\right)\right]}\sin\left(\psi_t + \Delta\psi_t\right) \end{aligned} \tag{30}$$

and

$$\begin{aligned} &w_w(-x, z, t + \frac{T_w}{2}) \\ =&-a_w\omega\frac{\cosh kz}{\sinh kh}\cos\phi\cosh kx\frac{-1 + \tan\phi\tan kx\tanh kz}{\cos\left[kx + \arctan\left(\tan\phi\tanh kz\right)\right]}\cos(\psi_n + \Delta\psi_n), \end{aligned} \tag{31}$$

where

$$\Delta\psi_t = 2\left[kx + \arctan\left(\frac{\tan\phi}{\tanh kz}\right)\right] + \pi \tag{32}$$

and

$$\Delta\psi_n = 2\left[kx + \arctan\left(\tan\phi\tanh kz\right)\right]. \tag{33}$$

By comparing (30) and (24) as well as (31) and (25), equations (28) and (29) are not always guaranteed due to the phase differences $\Delta\psi_t$ and $\Delta\psi_n$. Thus, $\{T(s,t),\ u(s,t),\ -w(s,t),\ -\phi(s,t)\}$ is not a solution to the governing equations (18) and (19) and therefore the blade motion is asymmetric. The phase differences lying within the interval $[-\pi, \pi)$ are given by

$$\boldsymbol{\Psi}_t = 2\left[kx + \arctan\left(\frac{\tan\phi}{\tanh kz}\right)\right] \text{ fmod } 2\pi - \pi \tag{34}$$

in the tangential direction and

$$\boldsymbol{\Psi}_n = \left\{2\left[kx + \arctan\left(\tan\phi\tanh kz\right)\right] + \pi\right\} \text{ fmod } 2\pi - \pi \tag{35}$$

in the normal direction, where the "fmod" operator is defined as $a \text{ fmod } b = a - nb$ and $n \in N$ such that $nb \leq a < (n+1)b$. The phase differences shown in equations (34) and (35) are explicitly expressed as functions of blade displacements, bending angle and wave number (representing wavelength), but implicitly functions of wave conditions and blade characteristics.

The phase differences consist of two terms corresponding to two major mechanisms that induce asymmetric motion, i.e., (i) the blade horizontal displacement ($kx$) and (ii) the action of vertical wave orbital velocity ($\tanh kz$, the ratio of vertical component to the horizontal component of wave orbital velocity) associated with blade vertical displacement ($kz$). The effects of bending angle ($\phi$) are not considered as a major mechanism because the term including $\tan\phi$ is dependent on the vertical wave orbital velocity. If the vertical wave orbital velocity does not exist, the effects of $\tan\phi$ will disappear. On the other hand, when $\phi > 45°$, $\tan\phi > 1$ acts as an amplification factor such that the action of vertical wave orbital velocity is more pronounced than the horizontal displacement of the blade.

Due to the phase differences in the encountered flow velocities, the drag and inertial forces are asymmetric, as well as the blade motion. The tangential phase difference $\boldsymbol{\Psi}_t$ describes the phase difference of the combined tangential force acting on the blade and driving the asymmetric blade motion. The tangential forces include friction and the tangential component of the virtual buoyancy. The normal phase difference $\boldsymbol{\Psi}_n$ describes the phase difference of the combined normal force acting on the blade and driving the asymmetric blade motion. The normal forces include drag, added mass force, and the normal component of the virtual buoyancy. In the case of

perfect symmetric blade motion, both $\mathbf{\Psi}_t$ and $\mathbf{\Psi}_n$ should equal zero at each time step. The onset of asymmetric motion will occur, however, relatively symmetric motion (defined as $\beta_{xT} \ll 1$) can occur when

$$|\mathbf{\Psi}_t| \ll 1 \tag{36}$$

and

$$|\mathbf{\Psi}_n| \ll 1. \tag{37}$$

The drag dominates compared to the frictional and inertial forces, so the normal forces are much larger than the tangential forces. Therefore, the contribution of normal phase difference $\mathbf{\Psi}_n$ to the asymmetric motion is expected to be much larger than that of tangential phase difference $\mathbf{\Psi}_t$. Thus, the motion is symmetric as long as equation (37) is satisfied.

Asymmetric blade motion is caused by the phase differences $\mathbf{\Psi}_t$ and $\mathbf{\Psi}_n$ of the encountered flow velocity due to the blade displacements. However, the magnitude of the asymmetry is also impacted by other factors including the blade characteristics and wave properties, which determine the blade displacements. The impacts of these factors on the magnitude of blade asymmetry will be further investigated using the cable model in the following sections.

### 4.3 Case study

The dynamic response of blades to symmetric wave forcing is investigated using the cable model. Blade geometric and material properties are adopted from those summarized in Lei and Nepf (2016), which are also provided in Table 3. In this case

**Table 3.** Blade geometric and material properties for the selected species used in the present study following Lei and Nepf (2016).

| | Elastic modulus $E$ (GPa) | Density $\rho_v$ (kg/m$^3$) | Thickness $d$ (mm) | Width $b$ (cm) | Length $l$ (m) | Flexural rigidity $EI$ ($\times 10^{-5}$ Nm$^2$) |
|---|---|---|---|---|---|---|
| *Thalassia testudinum** | $0.4 \sim 2.4$ | 940 | $0.30 \sim 0.37$ | 1 | $0.10 \sim 0.25$ | - |
| *Zostera marina*** | 0.26 | 700 | $0.15 \sim 0.23$ | $0.3 \sim 0.5$ | $0.15 \sim 0.60$ | - |
| *Posidonia oceanica**** | 0.47 | 910 | 0.20 | 1 | $0.15 \sim 0.50$ | - |
| Blades for case study | $0.1 \sim 0.3$ | 900 | 0.25 | 1 | $0.05 \sim 0.60$ | $0.13 \sim 3.9$ |

* Bradley and Houser (2009); Weitzman et al. (2013)
** Fonseca et al. (2007); Abdelrhman (2007); Moore (2004); McKone (2009)
*** Folkard (2005); Infantes et al. (2012)

study, the blade length $l = 0.05 \sim 0.60$ m and the flexural rigidity $EI = 0.13 \times 10^{-5} \sim 3.9 \times 10^{-5}$ Nm$^2$ are used to represent a variety of blade characteristics. Water depth is set as $h = 1$ m such that $l/h = 0.05 \sim 0.60$. Wave period $T_w = 0.9 \sim 12.2$ s is selected such that the ratio of water depth to wavelength is $h/L = 0.026 \sim 0.791$. This would correspond to a wide range of wave conditions from shallow to deep water. The wave height is set as $H/h = 0.02 \sim 0.30$ to consider the influence of wave heights on asymmetric motion. To make equations (12) to (14) applicable to calculate the hydrodynamic force coefficients, the selected results for analysis are from the cases with $\mathrm{KC} = 0.1 \sim 113.6$. The corresponding $\mathrm{Re} = 9.7 \sim 3822.5$ and $\mathrm{Ca} = 3.1 \sim 14742.8$.

To investigate the onset of asymmetric blade motion, $\mathbf{\Psi}_t$ and $\mathbf{\Psi}_n$ at the blade tip are calculated using the displacements and bending angles of the blade tip defined as $\mathbf{\Psi}_{tT}$ and $\mathbf{\Psi}_{nT}$, respectively. The results of the blade posture asymmetry ($\beta_{xT}$) are shown on Fig. 11, where waves propagate to the right such that $\beta_{xT} > 0$. The results

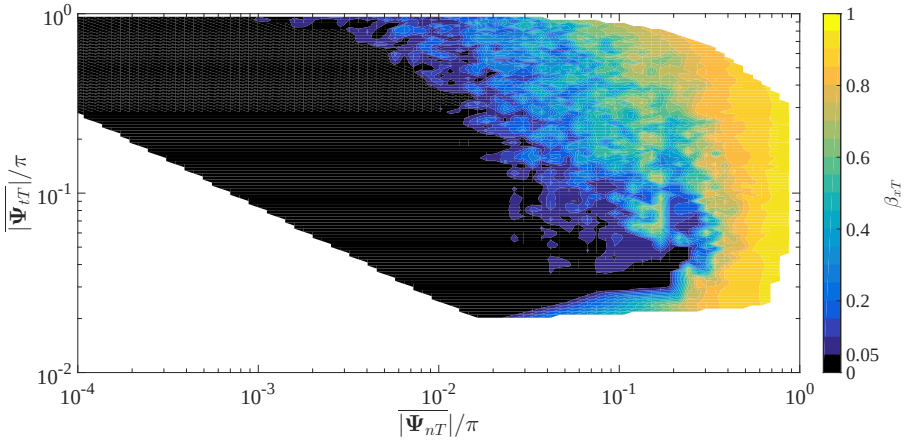


**Figure 11.** Contour of the blade posture asymmetry ($\beta_{xT}$, in colors) vs the normal phase difference $\mathbf{\Psi}_{nT}$ and tangential phase difference $\mathbf{\Psi}_{tT}$ at the blade tip. Waves propagate to the right such that $\beta_{xT} > 0$.

for the cases where waves propagate to the left are omitted here because $\beta_{xT}$ keeps the same magnitude but with an opposite sign. The blade motion is near symmetric ($\beta_{xT} < 0.05$) when $|\mathbf{\Psi}_{nT}|/\pi < 0.003$, regardless of the value of $\mathbf{\Psi}_{tT}$. if $|\mathbf{\Psi}_{tT}|/\pi < 0.3$, $\beta_{xT} < 0.05$ when $|\mathbf{\Psi}_{nT}|/\pi < 0.01$. Posture asymmetry increases with increasing $\mathbf{\Psi}_{tT}$ and $\mathbf{\Psi}_{nT}$. Ripples appear in the contours on Fig. 11 because $\mathbf{\Psi}_{tT}$ and $\mathbf{\Psi}_{nT}$ are the factors that only induce asymmetry. However, when the asymmetry occurs, the magnitude is influenced by the blade material and geometric characteristics, as well as the wave conditions.

The blade posture asymmetry is also examined as a function of the ratio of blade length to wave length ($\gamma = l/L$) for the wave conditions and blade characteristics shown on Fig. 12. The results show that the motion is almost symmetric ($\beta_{xT} < 0.05$) when $\gamma < 0.01$. As $\gamma$ increases, $\beta_{xT}$ increases to a peak value defined as peak asymmetry ($\beta_p$) and the corresponding $\gamma$ is defined as peak length ratio ($\gamma_p$), which characterizes the resonant condition. As shown on Fig. 12, $\beta_p$ increases with wave height and blade length. It is also evident that $\beta_p$ decreases with increasing blade flexural rigidity (Fig. 12a-d). However, for longer blades such that $l/h \geq 0.45$ as shown on Fig. 12(e) and (f), the decrease in $\beta_p$ is less than 5% for $H/h \geq 0.1$. This might be because long blades ($l/h \geq 0.45$) are so flexible that their postures are close to a bending limit. Near the limit, the posture changes slowly with flexural rigidity and so does the peak asymmetry. In general, the motion of a longer blade with smaller flexural rigidity in larger-amplitude waves behaves more asymmetric.

## 5 Discussion

### 5.1 Mechanisms for asymmetric blade motion

In symmetric waves, asymmetric blade motion is due to the phase differences of the encountered flow velocity and induced by two mechanisms: (i) the blade displacements and (ii) the vertical component of the wave orbital velocity. The effect of the vertical component of the orbital velocity is more pronounced than that of blade displacements, especially for a larger deflected blade with the posture being more horizontal. Previous research attributed the asymmetric motion to the wave orbital trajectory based on the assumption that the blade motion is at the same scale as the wave excursion (Döbken, 2015). However, the generalized mechanisms for the asym-

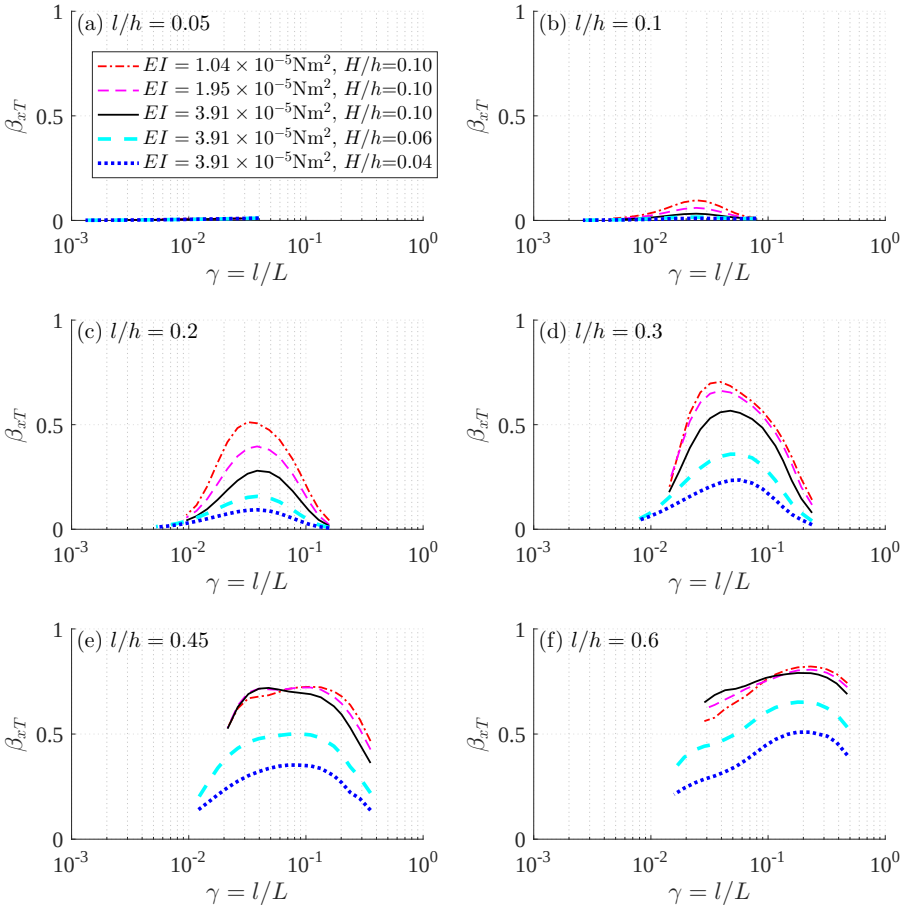


**Figure 12.** The blade posture asymmetry ($\beta_{xT}$) as a function of the ratio of blade length and wavelength ($\gamma = l/L$). The blade lengths normalized by water depth ($l/h$) are (a) 0.05, (b) 0.1, (c) 0.2, (d) 0.3, (e) 0.45 and (f) 0.6. The wave heights normalized by water depth ($H/h$) are 0.04, 0.06 and 0.1. The blade flexural rigidities ($EI$) are $1.04 \times 10^{-5}$, $1.95 \times 10^{-5}$ and $3.9 \times 10^{-5}$ Nm$^2$.

metric blade motion may be derived from the wave flow field relative to the blade motion without that assumption.

The blade postures as a function of wave orbital velocities at 8 wave phases over one wave period are shown on Fig. 13 (see Movie S2 for each time step in supporting information), where the waves propagate to the right. The blade is initially vertical at $t/T_w = 0$ and reaches steady state after up to 30 wave cycles. The steady state position of the blade is independent of its initial conditions. The blade motion is governed by the driving force and the bending stiffness of the blade. To simply demonstrate the underlying mechanisms, it is assumed that the driving force is dominated by drag and the blade velocity $(u, w)$ is smaller than the wave orbital velocity $(U, W)$ such that the force direction acts in the direction of the flow velocity $(U, W)$. For the steady scenario at position 0 under wave crest, the driving force is directed to the right following wave orbital velocity, which causes the blade to bend to the right (Fig. 13c). From position 0 to position 2, the horizontal component of wave orbital velocity $U$ is directed to the right in the direction of wave propagation, while the vertical component of wave orbital velocity $W$ points downward. From position 2 to 4, $U$ changes direction toward the left, but $W$ is still directed downward. Ultimately, there is a net force imposed on the blade due to $W$ acting downward on the blade for the first half of the wave cycle,

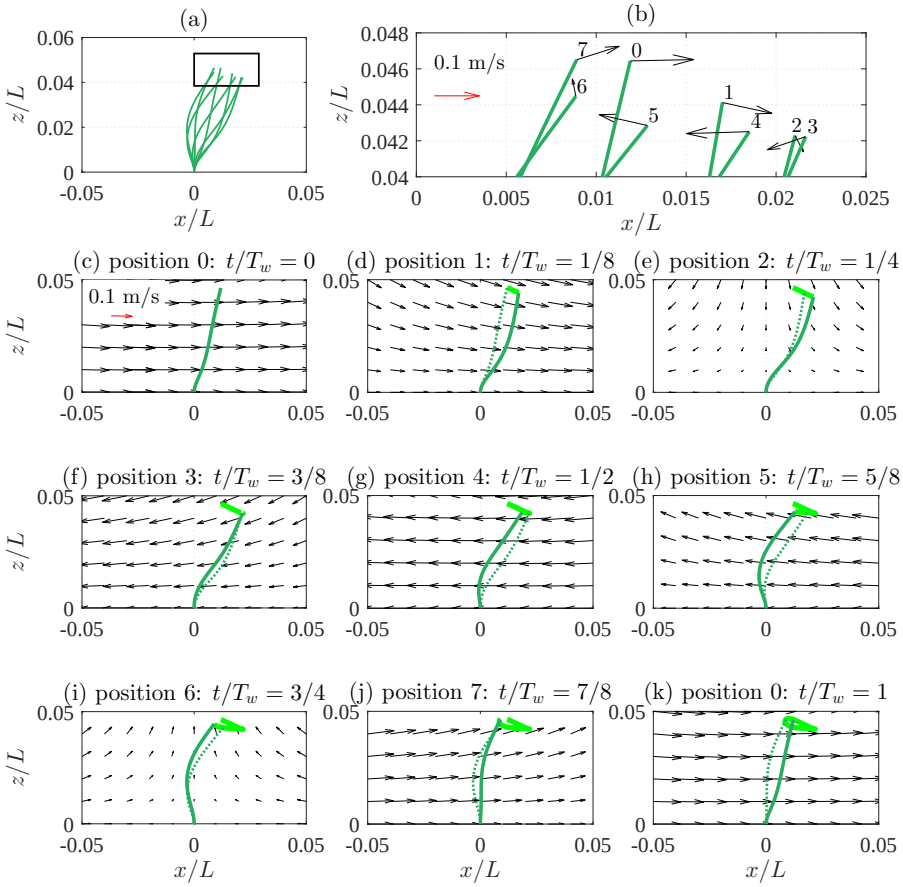


**Figure 13.** The postures of a 45 cm-long blade (in green) in the wave flow field with wave period $T_w = 3.2$ s and amplitude $a_w = 5$ cm in 1 m-deep water (intermediate water waves). The blade posture asymmetry is $\beta_{xT} = 0.7$. The waves propagate from left to right. The dark thin green lines indicate the blade postures. The blade displacements $(x, z)$ are normalized by wavelength $(L)$. (a) The blade postures from positions 0 to 7. (b) The upper parts (zoom in) of the blade postures labeled number 0 to 7, which indicate the blade positions at 8 wave phases with $t/T_w = 0$, 1/8, 1/4, 3/8, 1/2, 5/8, 3/4, 7/8, and 1 (see Movie S2 for each time step in supporting information). The black arrows indicate wave orbital velocity at the blade tip. (c) to (k) show the blade postures and wave flow field. The green solid line indicates the current blade posture and the dashed green lines indicate the blade posture at previous one position. The light thick green line indicate the trajectory of the blade tip. The black arrows indicate the wave flow field.

which promotes the downward motion of the blade and prevents it from moving back to position 0. In the second half of the wave period (positions 4 to 7), the blade begins slightly inclined to the right compared to position 0. Over the second half of the wave period, $U$ points to the left from positions 4 to 6 and changes direction toward the right from positions 6 to 0. However, $W$ is directed upward from positions 4 to 0, which prevents the downward motion of the blade on the left side of the vertical axis. The net effect of $W$ is a blade that is inclined in the direction of wave propagation.

Blade displacement influences the asymmetric flow velocity encountered by the blade. For example, by comparing $U$ during the second half of the wave period (position 4-7, Fig. 13g-j) with the first half (position 0-3, Fig. 13c-f), the positive horizontal

velocity $U$ towards the right is larger than the negative $U$ towards the left. Therefore, the net horizontal component is directed to the right, causing the blade to incline to the right.

Even though wave orbital velocities are symmetric over the wave period, blade inclination occurs due to the blade displacement and the asymmetric action of the vertical component of the wave orbital velocity. This inclination is more pronounced in shorter waves, as the vertical velocity increases to the same magnitude as the horizontal velocity, and the blade displacement becomes more comparable with the shortened wavelength.

### 5.2 Conditions for symmetric blade motion

Blade displacements and vertical wave orbital velocities induce blade asymmetry. Symmetric blade motion therefore occurs if these variables are very small, which are satisfied when (i) blade length is much smaller than the wavelength ($l/L \ll 1$), (ii) in shallow water waves ($h/L \ll 1$) and (iii) the blade length is much smaller than water depth ($l/h \ll 1$) in finite-depth-water waves. These conditions are derived from equations (36) and (37) and the detail derivations are provided in Appendix A.

For short blades in long waves ($l/L \ll 1$), the blade displacement and $W$ are negligible to the scale of wavelength so that phase differences between the encountered wave orbital velocities at asymmetric positions are also negligible, resulting in symmetric blade motion. Similarly, in shallow water waves ($h/L \ll 1$), the blade motion is symmetric because the effects of blade displacement and $W$ are negligible due to the small blade displacement compared to the wavelength and negligible $W$ in shallow water waves. One example of the symmetric blade motion in shallow water waves is shown on Fig. A1 (see Movie S3 for each time step in supporting information). For short blades ($l/h \ll 1$) in finite-depth-water waves ($h/L \sim \mathcal{O}(1)$), the blade motion behaves symmetric because the horizontal displacement of the blade is small, and $W$ is close to 0 when approaching the blade near the bottom. In the field, at the initial growth phase of SAV, the blade is so short that the motion is symmetric. When the blade grows longer, the blade motion may become asymmetric.

### 5.3 Properties and implications of asymmetric blade motion

Strict conditions for symmetric motion indicate that the occurrence of symmetric motion is limited. Therefore, the blade motion is typically asymmetric for most situations. The peak asymmetry occurs when the ratio of blade length to wavelength reaches the peak length ratio. The results showed that the peak asymmetry is a function of wave conditions and blade characteristics. Generally, the peak asymmetry of blade motion becomes larger in waves with a larger amplitude. When the blade grows longer, the peak asymmetry also increases because longer blade has larger deflection and encounters larger wave orbital velocities. However, the blade flexural rigidity reduces the peak asymmetry.

The behavior of asymmetric blade motion can be used to guide planting strategies of SAV for sediment settlement. The asymmetric motion is expected to benefit sediment settlement because the "shelter" created by the blade inclination could hinder sediment suspension at the seabed. To take advantage of the peak asymmetry, it is recommended to choose the SAV species such that the ratio of the blade length and the dominant wavelength is close to the peak length ratio. Longer blades are preferred because they increase the peak asymmetry and provide a larger "shelter".

The asymmetric blade motion may also influence the morphological characteristics and the fatigue life of SAV. The cross-section of the vegetation and even the elastic modulus may become asymmetric in response to the asymmetric blade motion.

For example, asymmetric motion induces the stress imbalance on the cross section. Thus, the tension side of the cross section becomes thinner while the compression side becomes thicker. Asymmetric blade motion and sheltering may lead to morphological change which in turn may affect flow pattern near the vegetation. The influences of asymmetric motion on the vegetation morphology and fatigue life will be investigated in the future work.

In the field, waves are usually superimposed with background currents (Weitzman et al., 2013, 2015). Following currents are expected to enhance the asymmetry of the blade motion while opposing currents are expected to decrease the asymmetry. With following currents, the asymmetry of blade motion increases with increasing currents (e.g., Fig. 6 of Lei & Nepf, 2019a).

A single vegetation blade likely has little influence on waves, however, numerous blades as a SAV meadow can significantly impact waves by generating turbulence (Abdolahpour et al., 2018; Zhang et al., 2018; Tang et al., 2019; Tan et al., 2019), reducing wave energy (Infantes et al., 2012; Paul et al., 2012; Henderson et al., 2017; Nowacki et al., 2017; Garzon et al., 2019), and inducing mean currents (Luhar & Nepf, 2011; Abdolahpour et al., 2017; Chen et al., 2019). The wave-driven currents in a vegetation meadow are expected to enhance the asymmetry of blade motion (e.g., Fig. 8 of Lei & Nepf, 2019b). In return, the asymmetric motion of blades as a meadow are likely to impact the wave-driven current and consequently the mass transport, which warrants further investigation. The asymmetric blade motion in a meadow is observed to modify the wave orbital velocity and further influence wave attenuation with a magnitude larger than the influences of blade stiffness (Paul et al., 2012). The wave shape may also be changed with the asymmetric blade motion due to the asymmetric wave attenuation.

## 6 Conclusions

The asymmetric behavior of SAV in waves was investigated using a mass-consistent cable model. Implementing the cable model improves blade motion modeling. This was especially true for "second-normal-mode-like" blade motion by incorporating the effects of the blade-motion-induced rotations of local Lagrangian coordinates along the blade on inertial force, the compatibility relations for geometrical continuity of the blade segments and the spatial variation of wave orbital velocity encountered by the blade due to blade displacements. With this cable model, two major factors were found to influence asymmetric blade motion other than wave orbital motion asymmetry. These factors are (i) the spatial asymmetry of the encountered wave orbital velocities induced by the blade displacements and (ii) the asymmetric action on the blade by the vertical wave orbital velocities. When near symmetric motion exists ($\beta_{xT} \ll 1$), conditions are (i) the blade length is much smaller than the wavelength with $l/L \ll 1$, (ii) in shallow water waves with $h/L \ll 1$ or (iii) the blade length is much smaller than the water depth with $l/h \ll 1$ in finite-depth-water waves. Peak asymmetry occurs when the ratio of blade length to wavelength ($l/L$) reaches the critical value. Peak asymmetry is found to increase with wave height and blade length but decrease with increasing blade flexural rigidity.

Asymmetric blade motion in a vegetation meadow is expected to influence the wave-driven currents, wave attenuation and wave shape. Meanwhile, the wave-driven currents and wave asymmetry also influence the asymmetry of blade motion. It is therefore worthwhile not only to investigate the dynamics of vegetation, but to also incorporate the two-way feedback between the asymmetric blade motion and the wave flow field in wave-vegetation models, such as the coupled CFD and immersed boundary method model by Chen and Zou (2019) and N-box model (Zeller et al., 2015). Improved blade posture simulations by the present consistent-mass cable model will yield

more accurate predictions for wave-vegetation interaction. In the future work, the cable model will be coupled with a 3D wave hydrodynamics model to investigate the capacity of SAV for wave attenuation, as well as its influence on wave-driven currents in a vegetation meadow.

## Appendix A Conditions for symmetric blade motion in symmetric waves

The absolute symmetric motion does not exist due to the phase differences $\mathbf{\Psi}_t$ and $\mathbf{\Psi}_n$. However, when $\mathbf{\Psi}_t$ and $\mathbf{\Psi}_n$ are close to 0, equations (28) and (29) hold such that $\{T(s,t), u(s,t), -w(s,t), -\phi(s,t)\}$ is also a solution to the governing equations (18) and (19), resulting in a relatively symmetric motion. Therefore, the conditions for relatively symmetric motion are obtained, i.e., $|\mathbf{\Psi}_t| \ll 1$ in (36) and $|\mathbf{\Psi}_n| \ll 1$ in (37).

According to equations (24) to (25) and (30) to (31), the wave orbital velocities at time $t$ and $t+T_w/2$ have the same amplitude. Therefore, the hydrodynamic coefficients $C_d$, $C_f$, and $C_m$ are the same at both positions, indicating that the hydrodynamic coefficients do not contribute to the generation of asymmetric motion. Generally, the driving forces in the normal direction dominate so that the contributions of $\mathbf{\Psi}_n$ to asymmetric motion is expected to be more significant and the tangential phase difference $\mathbf{\Psi}_t$ can be neglected due to the negligible forces in the tangential direction. Thus, the blade motion is symmetric when only equation (37) is satisfied.

For bottom-rooted blade configuration such that $|x| \le l$ and $|z| \le l$, it is evident that $kx + \arctan(\tan\phi \tanh kz) < kl + |\tan\phi \tanh kz| < (1 + |\tan\phi|)kl = 2\pi(1 + |\tan\phi|)l/L$. Since the blade cannot be fully horizontal, thus, $|\tan\phi|$ is finited. Therefore, one condition for $|\mathbf{\Psi}_n| \ll 1$ in (37) can be obtained,

$$l/L \ll 1. \tag{A1}$$

In fact, if $l/L \ll 1$, $\tanh kz \approx 0$ so that $|\mathbf{\Psi}_t| \approx 2kx < 4\pi l/L \ll 1$ such that equation (36) is also satisfied. Therefore, equation (A1) is one condition for symmetric blade motion. For completely submerged blades such that $l \le h$, then $l/L \le h/L$ so that the following condition for equation (A1) can be obtained,

$$h/L \ll 1, \tag{A2}$$

which is also a condition for symmetric blade motion. One example of blade symmetric motion in shallow water waves is shown on Fig. A1 (see Movie S3 for each time step in supporting information). In finite-water-depth waves with $h/L \sim \mathcal{O}(1)$, $l/L = h/L \cdot l/h \sim \mathcal{O}(l/h)$ so that the following condition for equation (A1) can be obtained,

$$l/h \ll 1, \tag{A3}$$

which is also a condition for symmetric blade motion.

## Acknowledgments

This work was completed as part of the PhD research of Longhuan Zhu who is supported by National Science Foundation award #IIA-1355457 to Maine EPSCoR at the University of Maine. The authors gratefully acknowledge the assistance of the Advanced Computing Group of the University of Maine System in producing and storing the numerical data, which are accessible through: `http://dataverse.acg.maine.edu/dvn/dv/SAV_Motion_In_Waves_JGR_Oceans`. The authors would like to sincerely thank Jeffrey Koseff for the guidance to get the data used on Fig. 2, Mitul Luhar and Heidi Nepf for providing the data used on Fig. 3-7 and Movie S1, and Dylan

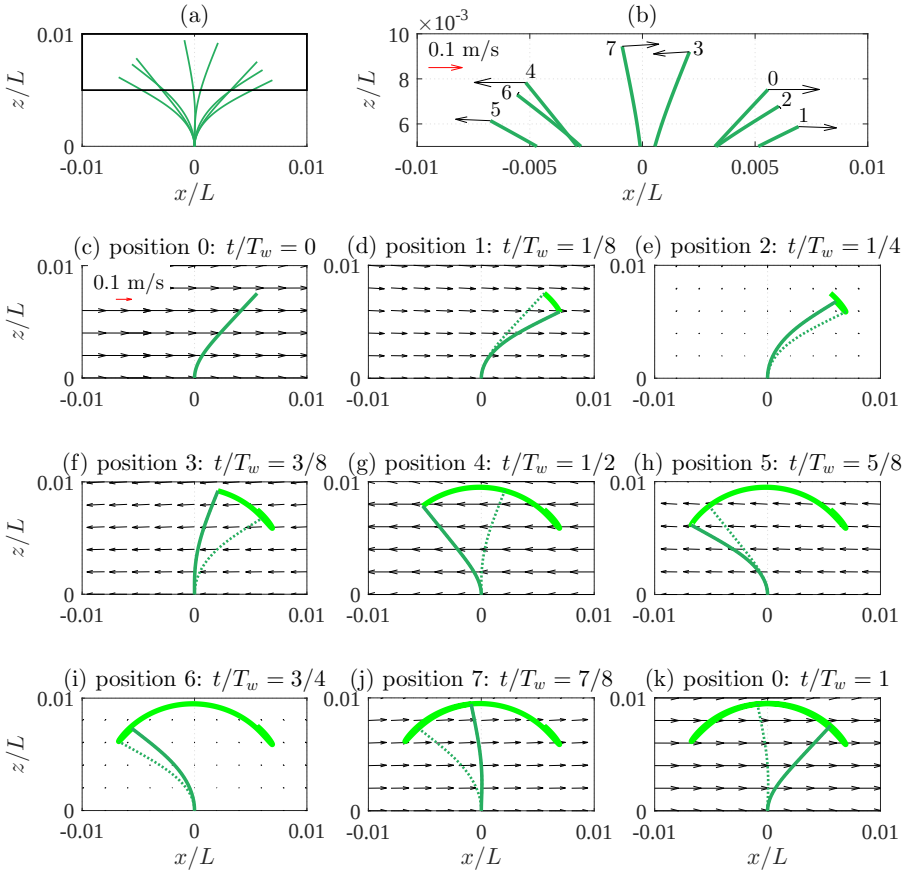


**Figure A1.** The postures of a 20 cm-long blade (in green) in the wave flow field with wave period $T_w = 6.8$ s and amplitude $a_w = 5$ cm in 1 m-deep water (shallow water waves). The blade posture asymmetry is $\beta_{xT} = 0.04$. The waves propagate from left to right. The dark thin green lines indicate the blade postures. The blade displacements $(x, z)$ are normalized by wavelength $(L)$. (a) The blade postures from positions 0 to 7. (b) The upper parts (zoom in) of the blade postures labeled number 0 to 7, which indicate the blade positions at 8 wave phases with $t/T_w = 0$, 1/8, 1/4, 3/8, 1/2, 5/8, 3/4, 7/8, and 1 (see Movie S3 for each time step in supporting information). The black arrows indicate wave orbital velocity at the blade tip. (c) to (k) show the blade postures and wave flow field. The green solid line indicates the current blade posture and the dashed green lines indicate the blade posture at previous one position. The light thick green line indicates the trajectory of the blade tip. The black arrows indicate the wave flow field.

Schlichting for reviewing the paper for style and grammar. The authors would also sincerely thank two anonymous reviewers for exceptionally constructive and helpful comments that greatly improved this manuscript.

## References

Abdelrhman, M. (2007). Modeling coupling between eelgrass Zostera marina and water flow. *Marine Ecology Progress Series*, *338*, 81–96. Retrieved from `http://www.int-res.com/abstracts/meps/v338/p81-96/` doi: 10.3354/meps338081

Abdolahpour, M., Ghisalberti, M., McMahon, K., & Lavery, P. S. (2018). The

impact of flexibility on flow, turbulence, and vertical mixing in coastal canopies. *Limnology and Oceanography*, *63*(6), 2777–2792. Retrieved from http://doi.wiley.com/10.1002/lno.11008 doi: 10.1002/lno.11008

Abdolahpour, M., Hambleton, M., & Ghisalberti, M. (2017). The wave-driven current in coastal canopies. *Journal of Geophysical Research: Oceans*, *122*(5), 3660–3674. Retrieved from http://doi.wiley.com/10.1002/2016JC012446 doi: 10.1002/2016JC012446

Anderson, D., Tannehill, J. C., & Pletcher, R. H. (2016). *Computational Fluid Mechanics and Heat Transfer, Third Edition*. CRC Press. Retrieved from https://www.taylorfrancis.com/books/9781466578302 doi: 10.1201/b12884

Arkema, K. K., Verutes, G. M., Wood, S. A., Clarke-Samuels, C., Rosado, S., Canto, M., ... Guerry, A. D. (2015). Embedding ecosystem services in coastal planning leads to better outcomes for people and nature. *Proceedings of the National Academy of Sciences*, *112*(24), 7390–7395. Retrieved from https://www.pnas.org/content/pnas/112/24/7390.full.pdf doi: 10.1073/pnas.1406483112

Bouma, T. J., De Vries, M. B., Low, E., Peralta, G., Tánczos, I. C., Van De Koppel, J., & Herman, P. M. (2005). Trade-offs related to ecosystem engineering: A case study on stiffness of emerging macrophytes. *Ecology*, *86*(8), 2187–2199. Retrieved from http://doi.wiley.com/10.1890/04-1588 doi: 10.1890/04-1588

Bradley, K., & Houser, C. (2009). Relative velocity of seagrass blades: Implications for wave attenuation in low-energy environments. *Journal of Geophysical Research*, *114*(F1), F01004. Retrieved from http://doi.wiley.com/10.1029/2007JF000951 doi: 10.1029/2007JF000951

Chatjigeorgiou, I. K. (2008). A finite differences formulation for the linear and nonlinear dynamics of 2D catenary risers. *Ocean Engineering*, *35*(7), 616–636. Retrieved from https://linkinghub.elsevier.com/retrieve/pii/S0029801808000085 doi: 10.1016/j.oceaneng.2008.01.006

Chen, H., Liu, X., & Zou, Q. (2019). Wave-driven flow induced by suspended and submerged canopies. *Advances in Water Resources*, *123*, 160–172. Retrieved from https://doi.org/10.1016/j.advwatres.2018.11.009 doi: 10.1016/j.advwatres.2018.11.009

Chen, H., & Zou, Q. (2019). Eulerian-Lagrangian flow-vegetation interaction model using immersed boundary method and OpenFOAM. *Advances in Water Resources*, *126*, 176–192. Retrieved from https://doi.org/10.1016/j.advwatres.2019.02.006 doi: 10.1016/j.advwatres.2019.02.006

Dalrymple, R. A., Kirby, J. T., & Hwang, P. A. (1984). Wave Diffraction Due to Areas of Energy Dissipation. *Journal of Waterway, Port, Coastal, and Ocean Engineering*, *110*(1), 67–79. Retrieved from http://ascelibrary.org/doi/10.1061/{\%}28ASCE{\%}290733-950X{\%}281984{\%}29110{\%}3A1{\%}2867{\%}29 doi: 10.1061/(ASCE)0733-950X(1984)110:1(67)

Dean, R. G., & Dalrymple, R. A. (1991). *Water Wave Mechanics for Engineers and Scientists* (Vol. 2; Intergovernmental Panel on Climate Change, Ed.) (No. 8). Cambridge: WORLD SCIENTIFIC. Retrieved from https://doi.org/10.1142/1232 doi: 10.1142/1232

Denny, M. W., Gaylord, B. P., & Cowen, E. A. (1997). Flow and flexibility II. The roles of size and shape in determining wave forces on the bull kelp Nereocystis luetkeana. *Journal of Experimental Biology*, *200*(24), 3165–3183. Retrieved from https://jeb.biologists.org/content/200/24/3165

Döbken, J. W. D. (2015). Modeling the interaction of wave hydrodynamics with flexible aquatic vegetation. *M.Sc. Thesis, Delft University of Technology*. Retrieved from http://citeseerx.ist.psu.edu/viewdoc/download?doi=10.1.1.970.1539{\&}rep=rep1{\&}type=pdf

Elgar, S., Freilich, M. H., & Guza, R. T. (1990). Model-data comparisons of moments of nonbreaking shoaling surface gravity waves. *Journal of Geophysical Research*, *95*(C9), 16055. Retrieved from http://doi.wiley.com/10.1029/JC095iC09p16055 doi: 10.1029/JC095iC09p16055

Folkard, A. M. (2005). Hydrodynamics of model Posidonia oceanica patches in shallow water. *Limnology and Oceanography*, *50*(5), 1592–1600. Retrieved from https://aslopubs.onlinelibrary.wiley.com/doi/pdf/10.4319/lo.2005.50.5.1592 doi: 10.4319/lo.2005.50.5.1592

Fonseca, M. S., Koehl, M., & Kopp, B. S. (2007). Biomechanical factors contributing to self-organization in seagrass landscapes. *Journal of Experimental Marine Biology and Ecology*, *340*(2), 227–246. Retrieved from https://linkinghub.elsevier.com/retrieve/pii/S0022098106005399 doi: 10.1016/j.jembe.2006.09.015

Garzon, J., Maza, M., Ferreira, C., Lara, J., & Losada, I. J. (2019). Wave attenuation by Spartina saltmarshes in the Chesapeake Bay under storm surge conditions. *Journal of Geophysical Research: Oceans*, 2018JC014865. Retrieved from https://onlinelibrary.wiley.com/doi/abs/10.1029/2018JC014865 doi: 10.1029/2018jc014865

Gaylord, B. P., Denny, M. W., & Koehl, M. A. (2003). Modulation of wave forces on kelp canopies by alongshore currents. *Limnology and Oceanography*, *48*(2), 860–871. Retrieved from https://aslopubs.onlinelibrary.wiley.com/doi/pdf/10.4319/lo.2003.48.2.0860 doi: 10.4319/lo.2003.48.2.0860

Ghisalberti, M., & Nepf, H. M. (2002). Mixing layers and coherent structures in vegetated aquatic flows. *Journal of Geophysical Research*, *107*(C2), 3011. Retrieved from http://doi.wiley.com/10.1029/2001JC000871 doi: 10.1029/2001JC000871

Gijón Mancheño, A. (2016). Interaction between wave hydrodynamics and flexible vegetation. *M.Sc. Thesis, Delft University of Technology*. Retrieved from http://resolver.tudelft.nl/uuid:bbaaf195-27e2-46ec-969c-603d6dd8f8c0

Guannel, G., Ruggiero, P., Faries, J., Arkema, K. K., Pinsky, M., Gelfenbaum, G., ... Kim, C. K. (2015). Integrated modeling framework to quantify the coastal protection services supplied by vegetation. *Journal of Geophysical Research: Oceans*, *120*(1), 324–345. Retrieved from http://doi.wiley.com/10.1002/2014JC009821 doi: 10.1002/2014JC009821

Henderson, S. M., Norris, B. K., Mullarney, J. C., & Bryan, K. R. (2017). Wave-frequency flows within a near-bed vegetation canopy. *Continental Shelf Research*, *147*, 91–101. Retrieved from https://linkinghub.elsevier.com/retrieve/pii/S0278434316305763 doi: 10.1016/j.csr.2017.06.003

Houser, C., Trimble, S., & Morales, B. (2015). Influence of Blade Flexibility on the Drag Coefficient of Aquatic Vegetation. *Estuaries and Coasts*, *38*(2), 569–577. Retrieved from https://link-springer-com.prxy4.ursus.maine.edu/content/pdf/10.1007{\%}2Fs12237-014-9840-3.pdfhttp://link.springer.com/10.1007/s12237-014-9840-3 doi: 10.1007/s12237-014-9840-3

Howell, C. T. (1992). *Investigation of the Dynamics of Low-Tension Cables* (Doctoral dissertation, Massachusetts Institute of Technology). Retrieved from http://www.dtic.mil/docs/citations/ADA268458

Hsieh, S.-R., Shaw, S. W., & Pierre, C. (1994). Normal modes for large amplitude vibration of a cantilever beam. *International Journal of Solids and Structures*, *31*(14), 1981–2014. Retrieved from https://deepblue.lib.umich.edu/bitstream/handle/2027.42/31489/0000411.pdf;sequence=1 doi: 10.1016/0020-7683(94)90203-8

Hu, J., Hu, Z., & Liu, P. L.-F. (2019). Surface water waves propagating over a submerged forest. *Coastal Engineering*, *152*, 103510. Retrieved from https://doi.org/10.1016/j.coastaleng.2019.103510 doi: 10.1016/j.coastaleng.2019

.103510

Hu, K., Chen, Q., Wang, H., Hartig, E. K., & Orton, P. M. (2018). Numerical modeling of salt marsh morphological change induced by Hurricane Sandy. *Coastal Engineering*, *132*, 63–81. Retrieved from https://doi.org/10.1016/j.coastaleng.2017.11.001 doi: 10.1016/j.coastaleng.2017.11.001

Hu, Z., Suzuki, T., Zitman, T., Uittewaal, W., & Stive, M. (2014). Laboratory study on wave dissipation by vegetation in combined currentwave flow. *Coastal Engineering*, *88*, 131–142. Retrieved from https://linkinghub.elsevier.com/retrieve/pii/S0378383914000416 doi: 10.1016/j.coastaleng.2014.02.009

Ikeda, S., Yamada, T., & Toda, Y. (2001). Numerical study on turbulent flow and honami in and above flexible plant canopy. *International Journal of Heat and Fluid Flow*, *22*(3), 252–258. Retrieved from https://linkinghub.elsevier.com/retrieve/pii/S0142727X0100087X doi: 10.1016/S0142-727X(01)00087-X

Infantes, E., Orfila, A., Simarro, G., Terrados, J., Luhar, M., & Nepf, H. M. (2012). Effect of a seagrass (Posidonia oceanica) meadow on wave propagation. *Marine Ecology Progress Series*, *456*, 63–72. Retrieved from http://www.int-res.com/abstracts/meps/v456/p63-72/ doi: 10.3354/meps09754

Jacobsen, N. G., Bakker, W., Uijttewaal, W. S. J., & Uittenbogaard, R. (2019). Experimental investigation of the wave-induced motion of and force distribution along a flexible stem. *Journal of Fluid Mechanics*, *880*, 1036–1069. Retrieved from https://www.cambridge.org/core/product/identifier/S0022112019007390/type/journal{_}article doi: 10.1017/jfm.2019.739

Keller, H. B. (1971). A new difference scheme for parabolic problems. In *Numerical solution of partial differential equations–ii* (pp. 327–350). Elsevier. Retrieved from https://linkinghub.elsevier.com/retrieve/pii/B9780123585028500141 doi: 10.1016/B978-0-12-358502-8.50014-1

Keulegan, G. H., & Carpenter, L. H. (1958). Forces on Cylinders and Plates in an Oscillating Fluid. *Journal of Research of the National Bureau of Standards*, *60*(5), 423–440. Retrieved from https://nvlpubs.nist.gov/nistpubs/jres/60/jresv60n5p423{_}A1b.pdf

Kobayashi, N., Raichle, A. W., & Asano, T. (1993). Wave Attenuation by Vegetation. *Journal of Waterway, Port, Coastal, and Ocean Engineering*, *119*(1), 30–48. Retrieved from http://ascelibrary.org/doi/10.1061/{\%}28ASCE{\%}290733-950X{\%}281993{\%}29119{\%}3A1{\%}2830{\%}29 doi: 10.1061/(ASCE)0733-950X(1993)119:1(30)

Leclercq, T., & de Langre, E. (2018). Reconfiguration of elastic blades in oscillatory flow. *Journal of Fluid Mechanics*, *838*, 606–630. Retrieved from https://www.cambridge.org/core/product/identifier/S0022112017009107/type/journal{_}article doi: 10.1017/jfm.2017.910

Lei, J., & Nepf, H. M. (2016). Impact of current speed on mass flux to a model flexible seagrass blade. *Journal of Geophysical Research: Oceans*, *121*(7), 4763–4776. Retrieved from http://doi.wiley.com/10.1002/2016JC011826 doi: 10.1002/2016JC011826

Lei, J., & Nepf, H. M. (2019a). Blade dynamics in combined waves and current. *Journal of Fluids and Structures*, *87*, 137–149. Retrieved from https://doi.org/10.1016/j.jfluidstructs.2019.03.020 doi: 10.1016/j.jfluidstructs.2019.03.020

Lei, J., & Nepf, H. M. (2019b). Wave damping by flexible vegetation: Connecting individual blade dynamics to the meadow scale. *Coastal Engineering*, *147*, 138–148. Retrieved from https://doi.org/10.1016/j.coastaleng.2019.01.008 doi: 10.1016/j.coastaleng.2019.01.008

Li, Y., Zhu, Q., Liu, L., & Tang, Y. (2018). Transient response of a SPAR-type floating offshore wind turbine with fractured mooring lines. *Renewable Energy*, *122*, 576–588. Retrieved from https://doi.org/10.1016/j.renene.2018.01

.067 doi: 10.1016/j.renene.2018.01.067

Lowe, R. J., Falter, J. L., Koseff, J. R., Monismith, S. G., & Atkinson, M. J. (2007). Spectral wave flow attenuation within submerged canopies: Implications for wave energy dissipation. *Journal of Geophysical Research: Oceans*, *112*(5), C05018. Retrieved from http://doi.wiley.com/10.1029/2006JC003605 doi: 10.1029/2006JC003605

Luhar, M. (2012). *Analytical and Experimental Studies of Plant-Flow Interaction at Multiple Scales* (Doctoral dissertation, Massachusetts Institute of Technology). Retrieved from http://dspace.mit.edu/handle/1721.1/78142

Luhar, M., Coutu, S., Infantes, E., Fox, S., & Nepf, H. M. (2010). Wave-induced velocities inside a model seagrass bed. *Journal of Geophysical Research: Oceans*, *115*(12), C12005. Retrieved from http://doi.wiley.com/10.1029/2010JC006345 doi: 10.1029/2010JC006345

Luhar, M., Infantes, E., & Nepf, H. M. (2017). Seagrass blade motion under waves and its impact on wave decay. *Journal of Geophysical Research: Oceans*, *122*(5), 3736–3752. Retrieved from http://doi.wiley.com/10.1002/2017JC012731 doi: 10.1002/2017JC012731

Luhar, M., Infantes, E., Orfila, A., Terrados, J., & Nepf, H. M. (2013). Field observations of wave-induced streaming through a submerged seagrass ( Posidonia oceanica ) meadow. *Journal of Geophysical Research: Oceans*, *118*(4), 1955–1968. Retrieved from http://doi.wiley.com/10.1002/jgrc.20162 doi: 10.1002/jgrc.20162

Luhar, M., & Nepf, H. M. (2011). Flow-induced reconfiguration of buoyant and flexible aquatic vegetation. *Limnology and Oceanography*, *56*(6), 2003–2017. Retrieved from http://doi.wiley.com/10.4319/lo.2011.56.6.2003 doi: 10.4319/lo.2011.56.6.2003

Luhar, M., & Nepf, H. M. (2016). Wave-induced dynamics of flexible blades. *Journal of Fluids and Structures*, *61*, 20–41. Retrieved from https://linkinghub.elsevier.com/retrieve/pii/S0889974615002613 doi: 10.1016/j.jfluidstructs.2015.11.007

Maza, M., Lara, J. L., Losada, I. J., Ondiviela, B., Trinogga, J., & Bouma, T. J. (2015). Large-scale 3-D experiments of wave and current interaction with real vegetation. Part 2: Experimental analysis. *Coastal Engineering*, *106*, 73–86. Retrieved from http://dx.doi.org/10.1016/j.coastaleng.2015.09.010 doi: 10.1016/j.coastaleng.2015.09.010

McKone, K. L. (2009). Light available to the seagrass zostera marina when exposed to currents and waves. *M.Sc. Thesis, University of Maryland, College Park*. Retrieved from https://drum.lib.umd.edu/bitstream/handle/1903/9352/McKone{_}umd{_}0117N{_}10401.pdf?sequence=1

Mendez, F. J., & Losada, I. J. (2004). An empirical model to estimate the propagation of random breaking and nonbreaking waves over vegetation fields. *Coastal Engineering*, *51*(2), 103–118. Retrieved from https://linkinghub.elsevier.com/retrieve/pii/S0378383903001182 doi: 10.1016/j.coastaleng.2003.11.003

Moore, K. A. (2004). Influence of Seagrasses on Water Quality in Shallow Regions of the Lower Chesapeake Bay. *Journal of Coastal Research*, *10045*(45), 162–178. Retrieved from http://www.bioone.org/doi/abs/10.2112/SI45-162.1 doi: 10.2112/SI45-162.1

Morison, J., Johnson, J., & Schaaf, S. (1950). The Force Exerted by Surface Waves on Piles. *Journal of Petroleum Technology*, *2*(05), 149–154. Retrieved from http://www.onepetro.org/doi/10.2118/950149-G doi: 10.2118/950149-G

Mullarney, J. C., & Henderson, S. M. (2010). Wave-forced motion of submerged single-stem vegetation. *Journal of Geophysical Research: Oceans*, *115*(12), C12061. Retrieved from http://doi.wiley.com/10.1029/2010JC006448 doi: 10.1029/2010JC006448

Nepf, H. M. (2012). Flow and Transport in Regions with Aquatic Vegetation. *Annual Review of Fluid Mechanics*, *44*(1), 123–142. Retrieved from http://www.annualreviews.org/doi/10.1146/annurev-fluid-120710-101048 doi: 10.1146/annurev-fluid-120710-101048

Nowacki, D. J., Beudin, A., & Ganju, N. K. (2017). Spectral wave dissipation by submerged aquatic vegetation in a back-barrier estuary. *Limnology and Oceanography*, *62*(2), 736–753. Retrieved from http://doi.wiley.com/10.1002/lno.10456 doi: 10.1002/lno.10456

Ondiviela, B., Losada, I. J., Lara, J. L., Maza, M., Galván, C., Bouma, T. J., & van Belzen, J. (2014). The role of seagrasses in coastal protection in a changing climate. *Coastal Engineering*, *87*, 158–168. Retrieved from https://linkinghub.elsevier.com/retrieve/pii/S0378383913001889 doi: 10.1016/j.coastaleng.2013.11.005

Paul, M., Bouma, T. J., & Amos, C. L. (2012). Wave attenuation by submerged vegetation: combining the effect of organism traits and tidal current. *Marine Ecology Progress Series*, *444*, 31–41. Retrieved from http://www.int-res.com/abstracts/meps/v444/p31-41/ doi: 10.3354/meps09489

Peng, Z., Zou, Q., Reeve, D., & Wang, B. (2009). Parameterisation and transformation of wave asymmetries over a low-crested breakwater. *Coastal Engineering*, *56*(11-12), 1123–1132. Retrieved from https://linkinghub.elsevier.com/retrieve/pii/S0378383909001264 doi: 10.1016/j.coastaleng.2009.08.005

Rao, S. S. (2010). *Mechanical vibrations (5th edition)*. Pearson.

Riffe, K. C., Henderson, S. M., & Mullarney, J. C. (2011). Wave dissipation by flexible vegetation. *Geophysical Research Letters*, *38*(18), n/a–n/a. Retrieved from http://doi.wiley.com/10.1029/2011GL048773 doi: 10.1029/2011GL048773

Rosman, J. H., Denny, M. W., Zeller, R. B., Monismith, S. G., & Koseff, J. R. (2013). Interaction of waves and currents with kelp forests (Macrocystis pyrifera): Insights from a dynamically scaled laboratory model. *Limnology and Oceanography*, *58*(3), 790–802. Retrieved from http://doi.wiley.com/10.4319/lo.2013.58.3.0790 doi: 10.4319/lo.2013.58.3.0790

Rupprecht, F., Möller, I., Paul, M., Kudella, M., Spencer, T., van Wesenbeeck, B., ... Schimmels, S. (2017). Vegetation-wave interactions in salt marshes under storm surge conditions. *Ecological Engineering*, *100*, 301–315. Retrieved from https://linkinghub.elsevier.com/retrieve/pii/S0925857416307443 doi: 10.1016/j.ecoleng.2016.12.030

Sarpkaya, T., & O'Keefe, J. L. (1996). Oscillating Flow About Two and Three-Dimensional Bilge Keels. *Journal of Offshore Mechanics and Arctic Engineering*, *118*(1), 1–6. Retrieved from https://asmedigitalcollection.asme.org/offshoremechanics/article/118/1/1/434651/Oscillating-Flow-About-Two-and-ThreeDimensional doi: 10.1115/1.2828796

Sparks, C. P. (2009). The Influence of Tension, Pressure and Weight on Pipe and Riser Deformations and Stresses. *Journal of Energy Resources Technology*, *106*(1), 46. Retrieved from http://energyresources.asmedigitalcollection.asme.org/article.aspx?articleid=1412283 doi: 10.1115/1.3231023

Suzuki, T., Hu, Z., Kumada, K., Phan, L. K., & Zijlema, M. (2019). Non-hydrostatic modeling of drag, inertia and porous effects in wave propagation over dense vegetation fields. *Coastal Engineering*, *149*, 49–64. Retrieved from https://doi.org/10.1016/j.coastaleng.2019.03.011 doi: 10.1016/j.coastaleng.2019.03.011

Tan, C., Huang, B., Liu, D., Qiu, J., Chen, H., Li, Y., & Hu, Z. (2019). Effect of Mimic Vegetation with Different Stiffness on Regular Wave Propagation and Turbulence. *Water*, *11*(1), 109. Retrieved from http://www.mdpi.com/2073-4441/11/1/109 doi: 10.3390/w11010109

Tang, C., Lei, J., & Nepf, H. M. (2019). Impact of a vegetationgenerated turbulence on the critical, nearbed, wavevelocity for sediment resuspension. *Water Resources Research*, 2018WR024335. Retrieved from https://doi.org/10.1029/https://onlinelibrary.wiley.com/doi/abs/10.1029/2018WR024335 doi: 10.1029/2018WR024335

Tjavaras, A., Zhu, Q., Lui, Y., Triantafyllou, M., D.K.P., Y., & Y. (1998). THE MECHANICS OF HIGHLY-EXTENSIBLE CABLES. *Journal of Sound and Vibration*, *213*(4), 709–737. Retrieved from https://doi.org/10.1006/jsvi.1998.1526

Triantafyllou, M., & Howell, C. (1994). Dynamic Response of Cables Under Negative Tension: an Ill-Posed Problem. *Journal of Sound and Vibration*, *173*(4), 433–447. Retrieved from https://linkinghub.elsevier.com/retrieve/pii/S0022460X84712399 doi: 10.1006/jsvi.1994.1239

Weitzman, J. S., Aveni-Deforge, K., Koseff, J. R., & Thomas, F. (2013). Uptake of dissolved inorganic nitrogen by shallow seagrass communities exposed to wave-driven unsteady flow. *Marine Ecology Progress Series*, *475*, 65–83. Retrieved from http://www.int-res.com/abstracts/meps/v475/p65-83/ doi: 10.3354/meps09965

Weitzman, J. S., Zeller, R. B., Thomas, F. I., & Koseff, J. R. (2015). The attenuation of current- and wave-driven flow within submerged multispecific vegetative canopies. *Limnology and Oceanography*, *60*(6), 1855–1874. Retrieved from http://doi.wiley.com/10.1002/lno.10121 doi: 10.1002/lno.10121

Zeller, R. B., Weitzman, J. S., Abbett, M. E., Zarama, F. J., Fringer, O. B., & Koseff, J. R. (2014). Improved parameterization of seagrass blade dynamics and wave attenuation based on numerical and laboratory experiments. *Limnology and Oceanography*, *59*(1), 251–266. Retrieved from http://doi.wiley.com/10.4319/lo.2014.59.1.0251 doi: 10.4319/lo.2014.59.1.0251

Zeller, R. B., Zarama, F. J., Weitzman, J. S., & Koseff, J. R. (2015). A simple and practical model for combined wavecurrent canopy flows. *Journal of Fluid Mechanics*, *767*, 842–880. Retrieved from https://www.cambridge.org/core/product/identifier/S0022112015000592/type/journal{_}article doi: 10.1017/jfm.2015.59

Zhang, Y., Tang, C., & Nepf, H. M. (2018). Turbulent Kinetic Energy in Submerged Model Canopies Under Oscillatory Flow. *Water Resources Research*, *54*(3), 1734–1750. Retrieved from http://doi.wiley.com/10.1002/2017WR021732 doi: 10.1002/2017WR021732

Zhu, L., & Chen, Q. (2015). Numerical Modeling of Surface Waves over Submerged Flexible Vegetation. *Journal of Engineering Mechanics*, *141*(8), A4015001. Retrieved from http://ascelibrary.org/doi/10.1061/{\%}28ASCE{\%}29EM.1943-7889.0000913 doi: 10.1061/(asce)em.1943-7889.0000913

Zou, Q., Hay, A. E., & Bowen, A. J. (2003). Vertical structure of surface gravity waves propagating over a sloping seabed: Theory and field measurements. *Journal of Geophysical Research: Oceans*, *108*(8), 3265. Retrieved from http://doi.wiley.com/10.1029/2002JC001432 doi: 10.1029/2002JC001432

Zou, Q., & Peng, Z. (2011). Evolution of wave shape over a low-crested structure. *Coastal Engineering*, *58*(6), 478–488. Retrieved from https://linkinghub.elsevier.com/retrieve/pii/S0378383911000020 doi: 10.1016/j.coastaleng.2011.01.001